



저작자표시-비영리-변경금지 2.0 대한민국

이용자는 아래의 조건을 따르는 경우에 한하여 자유롭게

- 이 저작물을 복제, 배포, 전송, 전시, 공연 및 방송할 수 있습니다.

다음과 같은 조건을 따라야 합니다:



저작자표시. 귀하는 원저작자를 표시하여야 합니다.



비영리. 귀하는 이 저작물을 영리 목적으로 이용할 수 없습니다.



변경금지. 귀하는 이 저작물을 개작, 변형 또는 가공할 수 없습니다.

- 귀하는, 이 저작물의 재이용이나 배포의 경우, 이 저작물에 적용된 이용허락조건을 명확하게 나타내어야 합니다.
- 저작권자로부터 별도의 허가를 받으면 이러한 조건들은 적용되지 않습니다.

저작권법에 따른 이용자의 권리는 위의 내용에 의하여 영향을 받지 않습니다.

이것은 [이용허락규약\(Legal Code\)](#)을 이해하기 쉽게 요약한 것입니다.

[Disclaimer](#)

이학석사학위논문

Characteristics of
Raindrop Size Distribution
Observed in Seoul

서울에서 관측된 빗방울 크기 분포의 특성

2020년 2월

서울대학교 대학원

지구환경과학부

좌민채

Abstract

The characteristics of raindrop size distribution (RSD) in Seoul are examined according to rain and weather types using Parsivel² disdrometer data collected from May 2018 to July 2019. Three rain types (convective, mixed, and stratiform) and six weather types (surface low-pressure system, upper-level trough, southwesterly flow, easterly flow, the Changma front, and typhoon) are considered. Among the rain types, the RSDs of stratiform rain shows the steepest slopes and the smallest mean mass-weighted diameters D_m , while the RSD of convective rain shows opposite characteristics. The logarithm of the mean generalized intercept parameter $\log_{10}N_w$ and the slope parameter Λ for stratiform rain show significantly broad distributions, which may be attributed to diverse forms of stratiform rain related to various weather types in Seoul. The RSD of mixed rain shows the mean values of D_m and Λ close to those of convective rain and the mean value of $\log_{10}N_w$ close to that of stratiform rain. The RSD characteristics also strongly depend on the weather type. The RSDs of surface low-pressure system and upper-level trough events exhibit steep slopes and small proportions of convective rain. In contrast, the RSDs of the Changma front and easterly flow events exhibit relatively modest slopes and relatively large proportions of convective rain. The large thermodynamic instability of these two weather types, as examined using the atmospheric sounding data and satellite data, is thought to be

responsible for the large proportion of convective rain. The exponent of the $Z-R$ power-law relation is the greatest for the Changma front events, which suggests that the rain intensity of this weather type highly depends on the production of large raindrops. The intercept parameter is determined according to the rain type following the power-law relationships for rainwater contents and is applied to a bulk microphysics scheme. It is found that the overall performance of the numerical model with the modified scheme has improved from that with the original scheme.

Keywords: Raindrop size distribution, Disdrometer, Rain type, Weather type, Seoul, WRF model, Parameterization

Student Number : 2017-28708

Contents

Abstract	i
Contents	ii
List of Figures	iii
List of Tables	iv
1. Introduction	1
2. Data and Methods	5
2.1. Data	5
2.2. Methods	14
2.2.1. Description of parameters	14
2.2.2. Rain-type classification	17
2.2.3. Weather-type classification	18
3. Results	21
3.1. Characteristics of RSDs according to rainrate	21
3.2. Characteristics of RSDs according to different rain types	26
3.3. Characteristics of RSDs according to different weather types	31
3.4. Application to the numerical models	47
3.4.1. Parameterization of the intercept parameter	47
3.4.2. Experiment settings	52
3.4.3. Numerical model results	57
4. Summary and Discussions	63
References	67
초 록	77

List of Figures

- Figure 1.** Photo of OTT Parsivel² disdrometer installed on the roof of the Atmospheric Environmental Observatory building, Seoul National University. 6
- Figure 2.** Accumulated rain amount (grey bar) and accumulated rain duration (black solid line) for each rain rate category for the observation period..... 8
- Figure 3.** Daily accumulated precipitation amounts measured by the Parsivel² and the AWS rain gauge for each precipitation event that occurred for the observation period. 11
- Figure 4.** Daily accumulated precipitation amount measured by the Parsivel² disdrometer versus that measured by the AWS rain gauge. The red dashed line indicates $y = x$ 12
- Figure 5.** Accumulated number of drops by fall velocity and diameter for the observation period: (a) before and (b) after the quality control. The solid line indicates the fall velocity-diameter relationship of Atlas et al. (1973). The dashed lines indicate the $\pm 60\%$ of the fall velocity-diameter relationship. 13
- Figure 6.** Synoptic weather charts at 850-hPa level describing each weather type. (a) surface low-pressure system at 15 LST 6 May 2018, (b) upper-level trough at 15 LST 26 Oct 2018, (c) southwesterly flow at 15 LST 24 Jul 2019, (d) easterly flow at 15 LST 28 Jul 2018, (e) Changma front at 21 LST 29 Aug 2018, and (f) typhoon at 15 LST 24 Aug 2018. The blue solid lines and the red dashed lines represent geopotential height and isotherm, respectively. The

weather charts are depicted using European Centre for Medium-Range Weather Forecasts (ECMWF) Interim Re-Analysis (ERA-Interim) 6-hourly data.20

Figure 7. Raindrop size distributions (solid lines) and corresponding exponential distribution (dashed lines) for each rain rate category for the observation period.22

Figure 8. (a) Slope parameter and (b) intercept parameter for each rain rate category.....23

Figure 9. Scatterplots of D_0 and $\log_{10}N_w$ for rain case 1 to rain case 9. The black solid line represents the separator line of Bringi et al. (2009).25

Figure 10. Raindrop size distributions for each rain case during (a) stratiform rain (case 1, case 2, and case 3), (b) mixed rain (case 4, case 5, and case 6), and (c) convective rain cases (case 7, case 8, and case 9).29

Figure 11. Probability density functions of (a) D_m , (b) $\log_{10}N_w$, (c) Λ , and (d) Z for each rain type.....30

Figure 12. Raindrop size distributions for each weather type (L: surface low-pressure system, UT: upper-level trough, SW: southwesterly flow, E: easterly flow, CF: Changma front, and T: typhoon).32

Figure 13. Probability density functions of (a) D_m , (b) $\log_{10}N_w$, (c) Λ , and (d) Z for each weather type (L: surface low-pressure system, UT: upper-level trough, SW: southwesterly flow, E: easterly flow, CF: Changma front, and T: typhoon).33

Figure 14. Boxplot of $D_m - \log_{10} N_w$ pairs (medians with 10th and 90th percentiles) for each weather type (L: surface low-pressure system, UT: upper-level trough, SW: southwesterly flow, E: easterly flow, CF: Changma front, and T: typhoon). The black dashed line represents the stratiform line in Bringi et al. (2003). The two gray boxes indicate the maritime and continental convective clusters, respectively, reported by Bringi et al. (2003). 38

Figure 15. Scatterplot of $Z-R$ pairs for each weather type (L: surface low-pressure system, UT: upper-level trough, SW: southwesterly flow, E: easterly flow, CF: Changma front, and T: typhoon). The fitted power-law relationship $Z = aR^b$ for each weather type are indicated by black, blue, cyan, green, red, and magenta solid lines, respectively. 39

Figure 16. Skew T–log p diagrams of Osan station soundings during the event of (a) surface low-pressure system at 09 LST 6 May 2018, (b) easterly flow at 21 LST 28 Jul 2018, and (c) Changma front at 21 LST 29 Aug 2018. The solid red and blue lines are temperature and dew point temperature profiles, respectively. The brown line indicates the moist adiabatic lapse rate connecting LFC and EL. Wind barbs are plotted on the right side of the soundings. 45

Figure 17. Cloud-top temperature (K) for the same event of figure 16 using National Meteorological Satellite Center (NMSC) COMS data. 46

Figure 18. Intercept parameter as a function of (a) rainwater content and (b) slope parameter for the entire 1-min rain samples (black dots). Red lines represent fitted power law equations. 49

Figure 19. Intercept parameter as a function of rainwater content for (a) stratiform, (b) mixed, and (c) convective rain. Red lines represent fitted power

law equations.....50

Figure 20. Illustration of three nested model domains with terrain height.53

Figure 21. Fields of 850 hPa equivalent potential temperature (K, shaded) and horizontal wind vector (m s^{-1} , arrows) at (a) Aug 29 03 LST, (c) Aug 29 15 LST and (e) Aug 30 03 LST using the National Centers for Environmental Prediction (NCEP) Final (FNL) 0.25-degree analysis data. Same for (b), (d), (f) but from simulation results.....55

Figure 22. (a) Spatial distributions of the surface precipitation amount accumulated over the 57-h period of TRMM satellite observations and (b) AWS observations, and (c) ~ (f) WRF simulation results for four different R and W options.59

Figure 23. The Brier score for the 57-h accumulated precipitation amount of each R and W option (Option1~4) across the range of thresholds. The Brier score for WSM6 scheme is also depicted for comparison.....60

Figure 24. (a) Spatial distributions of the surface precipitation amount accumulated over the 24-h period of TRMM satellite observations, (b) AWS observations, (c) WSM6 scheme, and (d) WSM6 modified scheme.....61

Figure 25. The Brier score for the 24-h accumulated precipitation amount of each parameterization (WSM6 scheme and WSM6 modified scheme) across the range of thresholds.....62

List of Tables

Table 1. Rain case number, period, rain duration, amount, type and weather type for the nine different cases (S: stratiform rain, M: mixed rain, C: convective rain).	24
Table 2. Mean (μ), standard deviation (σ), kurtosis (k), and skewness (s) of D_m , $\log_{10}N_w$, Λ , and Z PDFs for different weather types. Squared brackets indicate averaging over the PDF of all daily rain events classified according to weather types.....	34
Table 3. Mean values of lifted condensation level (LCL), level of free convection (LFC), equilibrium level (EL), convective available potential energy (CAPE), and precipitable water calculated from 368 Osan station soundings of each weather type.....	44
Table 4. Domain configuration and physics schemes used in this study. .	51
Table 5. Description of intercept parameter types and corresponding value /equations.....	54

1. Introduction

Knowing the drop size distribution (DSD) of precipitating particles is essential to understanding the microphysical processes involved in precipitation since DSD varies with the physical processes associated with precipitation formation (Rosenfeld & Ulbrich, 2003), DSD observations, therefore, have found uses in examining precipitation characteristics, microphysical processes, and spatiotemporal variability of DSD (Bringi et al., 2003; Ulbrich & Atlas, 2007; Bringi et al., 2009; Jaffrain & Berne, 2011; Chen et al., 2012; You & Lee, 2015; Ghada et al., 2018; Wen et al., 2019). Analyzing the DSD and its variability for a precipitation event can also be helpful in improving the accuracy of quantitative precipitation forecasts, the parameterizations of microphysical processes in numerical models (Zhang et al., 2006), and the estimation of soil erosion (Wen et al., 2019).

DSDs can be directly observed with a surface disdrometer. In addition to DSD, surface disdrometers provide additional information about precipitating particles such as their shapes as well as various other physical properties (Chang et al., 2009; Thurai et al., 2016). Given the advantages of using a surface disdrometer such as easy installation and maintenance, high hardware durability, and relatively low cost, there have sprung up many surface disdrometer-based studies that track the spatiotemporal changes in the precipitation characteristics over small areas (e.g., Tokay & Short, 1996; Tapiador et al., 2010).

More specifically, many studies have used raindrop size distribution (RSD) observations to study the relationship between RSD variations and relevant factors such as topography, climatic region, season, rain type, and weather type. Gao et al. (2018) examined the topographic effect of the Tibetan Plateau on the RSD of convective rain and found that raindrops observed at higher altitudes have larger mean diameters than raindrops observed at lower altitudes due to a decrease in the collisional breakup process. Massmann et al. (2017) compared the characteristics of warm rain and ice-initiated rain over Chile's Nahuelbuta Mountains using the RSD obtained from a Parsivel disdrometer. They found that warm rain over the mountains consisted of a relatively larger number of small raindrops and had a slightly smaller liquid water content and a weaker rain intensity. Other studies have analyzed the characteristics of RSDs in different climatic regions such as the mid-latitudes, and the tropical equatorial, oceanic, and continental regions (Tokay & Short, 1996; Kozu et al., 2005; Ulbrich & Atlas, 2007; Montopoli et al., 2008; Leinonen et al., 2012; Tenorio et al., 2012; Thompson et al., 2015). Wen et al. (2019) analyzed the seasonal variability of RSD obtained from a 2-D video disdrometer in East China. They found that summer rain is mostly composed of convective rain with maritime origin and that the derived relations of the RSD parameters for four seasons are clearly different from each other. Sreekanth et al. (2019) compared the characteristics of different rain types in winter, pre-monsoon, summer monsoon, and post-monsoon seasons in tropical regions using the RSD obtained from impact-type disdrometers. They

showed that transition and mixed rain contribute significantly to the total amount of rain, especially during the summer monsoon season. In this study, we focus on both rain and weather types and how they influence the RSD characteristics in Seoul, South Korea. Zhang et al. (2017) examined the RSD characteristics corresponding to different life stages of a midlatitude continental squall line. They found that the RSD characteristics vary greatly depending on the type of rain and the life stage of the squall line. Hachani et al. (2017) examined the characteristics of the RSD according to the latitude, season, synoptic weather pattern, topography, and rain type and found that most of these factors except for the distance from the sea influence the RSD characteristics in the Cévennes-Vivarais region, France.

The Korean Peninsula is affected by a diversity of weather phenomena, affected by the mountainous terrains or the proximity to the seas. For this reason, the conditions can differ from region to region, Suh et al. (2016) analyzed the RSD characteristics in Busan for ten different rain categories covering different temporal and spatial scales. Loh et al. (2019) compared the RSD characteristics observed in Jincheon and Miryang according to the three weather types they identified for these regions. To the best of the author's knowledge, however, there has not been a study analyzing the characteristics of RSD according to both rain and weather types in Seoul. Since Seoul is a densely-populated city with a population of approximately 10 million people in an area of about 600 km², precipitation here can have a huge impact on society.

Applying the analysis results of the rain characteristics to a numerical model likely will improve the simulation performance. Zhang et al. (2008) used the RSD observations from Oklahoma to calculate the RSD parameters and applied them to numerical models to improve the accuracy of quantitative precipitation estimates. In Zhang et al. (2008), however, the relationship between the intercept parameters and rainwater content for convective rain events obtained from the disdrometer observations was applied to the Kessler parameterization scheme to calculate the evaporation rate, accretion rate, terminal velocity, and reflectivity factor. Their results were compared with the original scheme but have not been experimented on real case simulations. Recently, there have been some efforts (by the KMA) to use disdrometer observations to improve the precipitation estimation performance in the Korean Peninsula, but the results have yet to be released. The purpose of this study is to analyze the RSD characteristics in Seoul using a Parsivel² disdrometer and examine how these characteristics vary according to rain and weather types. In addition, the RSD analysis results are applied to a bulk microphysics scheme, and the possibility of improvement of the quantitative precipitation estimation is supported by comparing the simulated precipitation amount over the Korean Peninsula with the modified model and the original model in real case simulations. Section 2 includes descriptions of the Parsivel² disdrometer used in this study, as well as the data and methodology. The analysis results are presented and the numerical simulation results are discussed in Section 3. A summary and conclusions are given in

Section 4.

2. Data and Methods

2.1. Data

The disdrometer used in this study is the Parsivel² disdrometer manufactured by OTT Hydromet of Germany and is installed at Seoul National University (Figure 1). The Parsivel disdrometer measures the diameter and fall velocity of hydrometeor particles that fall through the horizontal laser beam of 1 mm thickness with a sampling area of 54 cm² (180 mm long and 30 mm wide) and a wavelength of 650 nm and a maximum output of 0.2 mW. It also outputs variables such as hydrometeor type, kinetic energy, precipitation intensity, and the radar reflectivity factor. The fall velocity is calculated based on the duration of time within which the signal is blocked by the hydrometeors passing through the sampling area, and the particle diameter is measured from the magnitude of the attenuated signal. The raw output provides the number of drops in a 32 × 32 size versus fall velocity matrix, and the sampling output interval is 1 min. The two smallest size classes are excluded from the analysis following the manufacturer's recommendation citing the low signal-to-noise ratio (Tokay et al., 2014). As



Figure 1. Photo of OTT Parsivel² disdrometer installed on the roof of the Atmospheric Environmental Observatory building, Seoul National University.

a result, the available particle sizes range from 0.25 to 26 mm. The calculated fall velocities range from 0 to 22.4 m s⁻¹. The measurement accuracy for the particle diameter reported by the manufacturer is within ±1 size class up to 2 mm and ±0.5 size class above 2 mm. The accuracy of the calculated precipitation intensity of the liquid drops is within ±5%.

In this study, the observation data from 3 May 2018 to 31 July 2019 are analyzed. Figure 2 shows the accumulated rain amount and accumulated rain duration for different rain intensity (R) categories during the observation period. The two weakest R categories ($R < 5 \text{ mm h}^{-1}$) account for 90.8% of the total rain duration, and 45.0% of the total rain amount; the two strongest rain intensity categories ($R > 20 \text{ mm h}^{-1}$) account for 1.4% of the total rain duration and 23.4% of the total rain amount. The largest contributor to the rain amount is the second category ($2 \leq R < 5 \text{ mm h}^{-1}$), which accounts for 16.5% of the total rain duration and 24.2% of the total rain amount. Rain accounts for 96.6% of the rain duration and 63.6% of the rain amount when R less than 10 mm h^{-1} , and 98.6% and 76.6%, respectively when R is less than 20 mm h^{-1} .

To evaluate the reliability of the observations, the daily accumulated precipitation data from the Parsivel² disdrometer and the automatic weather station (AWS) rain gauge located ~4 m away from the Parsivel² disdrometer are compared. The measurement accuracy of the AWS rain gauge is within

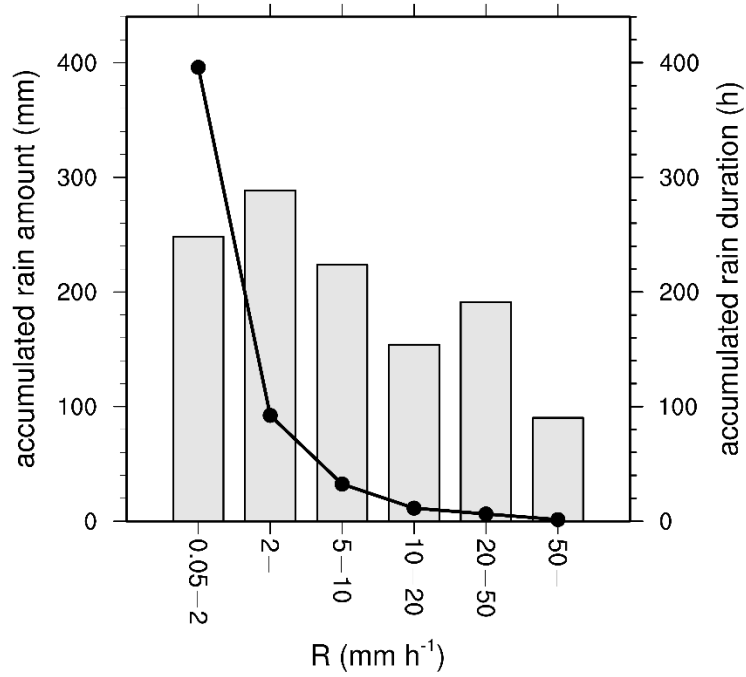


Figure 2. Accumulated rain amount (grey bar) and accumulated rain duration (black solid line) for each rain rate category for the observation period.

± 0.5 mm for $0 < R < 20$ mm h⁻¹ and $< 3\%$ for $R > 20$ mm h⁻¹ according to the Korea Meteorological Administration (KMA).

The comparison of the daily accumulated precipitation amount between the Parsivel² disdrometer and the AWS rain gauge for each precipitation event is shown in Figure 3. Figure 4 is a scatterplot of the daily accumulated precipitation amount measured by the Parsivel² disdrometer and the AWS rain gauge. Figures 3 and 4 show that the daily accumulated precipitation amount obtained from the Parsivel² disdrometer and the AWS rain gauge are well matched. In some events, the Parsivel² disdrometer tends to underestimate the precipitation amount because some small drops are hidden behind larger drops and are not detected by the laser beam (Wen et al., 2017) especially when precipitation intensity is strong. Since the regression coefficient R^2 is greater than 0.99 and the number of underestimated events is small, the observation data from the Parsivel² disdrometer are deemed reliable.

Before using the Parsivel² data, a quality control process that removes the observation errors is performed. According to Friedrich et al. (2013), the main factors of the measurement inaccuracies of Parsivel² are misclassifications of precipitation particles caused by (1) strong winds, (2) particles falling at the edges of the sampling area (Yuter et al., 2006), and (3) splashing effects from particles falling on the head surface of the machine. First, the inaccuracies caused by strong winds are remedied by removing particles with diameters larger than 5 mm and fall velocities smaller than 1 m

s⁻¹. Second, to eliminate inaccuracies caused by the marginal effect, particles with diameters less than 8 mm and whose fall velocities are 60% greater than that following the fall velocity-diameter relationship of Atlas et al. (1973), corresponding to the solid lines in Figures 5a and 5b, are excluded (Jaffrain & Berne, 2011). Finally, the inaccuracies due to the splashing effect are eliminated by excluding particles smaller than 2 mm in diameter and less than 60% of the fall velocity-diameter relation (Barthazy et al., 2004; Krajewski et al., 2006; Yuter et al., 2006). All data involving snow and hail particles are removed.

Following Thompson et al. (2015), only the data (which were collected every minute) with $R > 0.05 \text{ mm h}^{-1}$ and that have a total particle count of 100 or more during three consecutive minutes of precipitation are considered. Additionally, both rain and drizzle are treated as rain. In the end, the data used for the analyses consist of a total of 100 rain events and 34,6541-minute interval data entries.

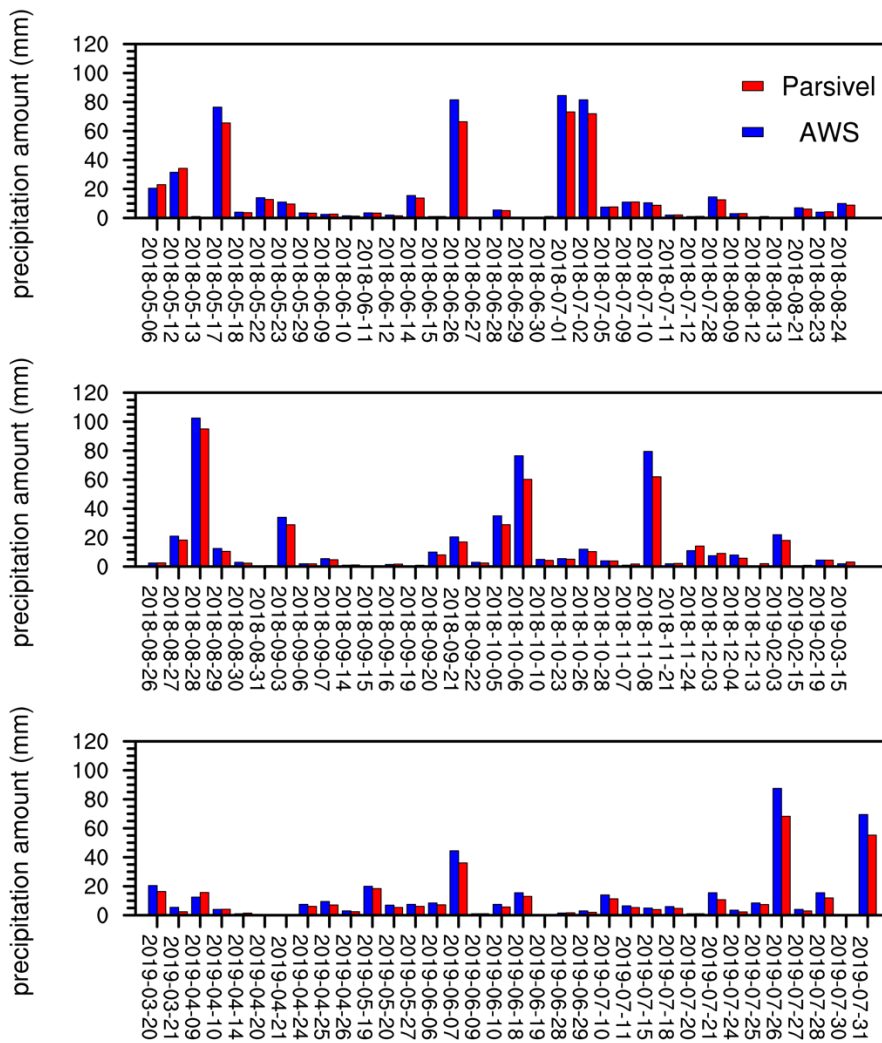


Figure 3. Daily accumulated precipitation amounts measured by the Parsivel² and the AWS rain gauge for each precipitation event that occurred for the observation period.

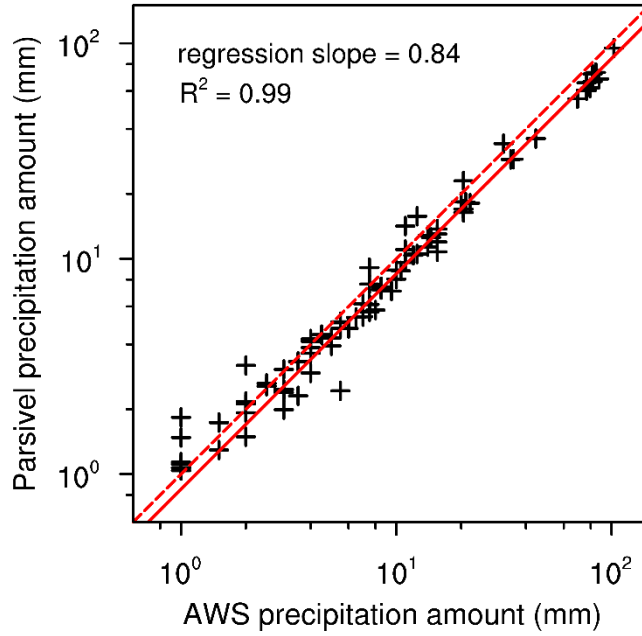


Figure 4. Daily accumulated precipitation amount measured by the Parsivel² disdrometer versus that measured by the AWS rain gauge. The red dashed line indicates $y = x$.

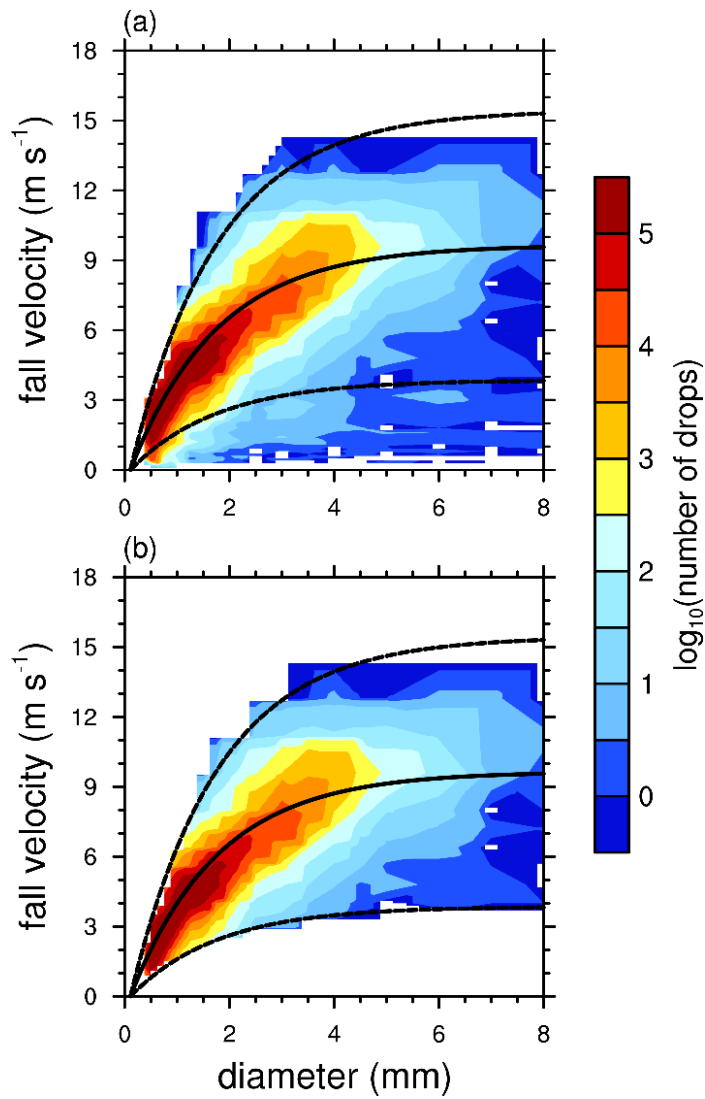


Figure 5. Accumulated number of drops by fall velocity and diameter for the observation period: (a) before and (b) after the quality control. The solid line indicates the fall velocity-diameter relationship of Atlas et al. (1973). The dashed lines indicate the $\pm 60\%$ of the fall velocity-diameter relationship.

2.2. Methods

2.2.1. Description of parameters

Using the disdrometer data, the raindrop concentration $N(D)$ ($\text{m}^{-3} \text{mm}^{-1}$) can be obtained from the following equation (Chen et al., 2017):

$$N(D_i) = \sum_{j=1}^{32} \frac{n_{ij}}{A_i V_j \Delta t \Delta D_i}, \quad (1)$$

where $N(D_i)$ ($\text{m}^{-3} \text{mm}^{-1}$) is the number concentration of raindrops per unit volume in the diameter range D_i to $D_i + \Delta D_i$ (mm), n_{ij} is the number of raindrops belonging to size class i and speed class j , V_j (m s^{-1}) is the fall velocity of speed class j , A_i (m^2) is the effective sampling area of size class i , and Δt (s) is the sampling time interval, which is 60 s in this study. Additional integral parameters obtained from $N(D_i)$ include rainwater content W (g m^{-3}) and radar reflectivity factor Z (whose values are by convention given in terms of the $\text{mm}^6 \text{m}^{-3}$ unit), which are represented by the following equations:

$$W = \frac{\pi}{6} \rho_w \int D^3 N(D) dD = \frac{\pi}{6} \rho_w \sum_{i=3}^{32} \sum_{j=1}^{32} D_i^3 \frac{n_{ij}}{A_i V_j \Delta t}, \quad (2)$$

$$Z = \int D^6 N(D) dD = \sum_{i=3}^{32} \sum_{j=1}^{32} D_i^6 \frac{n_{ij}}{A_i V_j \Delta t}, \quad (3)$$

where ρ_w (g cm^{-3}) is the density of water. The k th-order moments for the RSD are written as

$$M_k = \int D^k N(D) dD = \sum_{i=3}^{32} D_i^k N(D_i) \Delta D_i. \quad (4)$$

The mass-weighted mean diameter D_m (mm) and generalized intercept parameter N_w ($\text{m}^{-3} \text{mm}^{-1}$) are calculated using the equations

$$D_m = \frac{M_3}{M_4}, \quad (5)$$

$$N_w = \frac{4^4}{\pi \rho_w} \left(\frac{10^3 W}{D_m^4} \right). \quad (6)$$

The most commonly used function to express RSD is the probability density function of the exponential distribution (shortened as the exponential distribution function hereafter), which is expressed as $N(D) = N_0 \exp(-\Lambda D)$, where N_0 is the intercept parameter ($\text{m}^{-3} \text{mm}^{-1}$) and Λ is the slope parameter (mm^{-1}). The parameter N_0 is generally assigned a fixed value, a representative example of which is $N_0 = 8 \times 10^3 \text{ m}^{-3} \text{mm}^{-1}$ in Marshall & Palmer (1948, MP48 hereafter). The exponential distribution is a special case of the gamma distribution (Ulbrich, 1983) with $\mu = 0$, whose probability

density function is given by $N(D) = N_0 D^\mu \exp(-\Lambda D)$. The parameters for the gamma distribution μ , Λ , and N_0 can be expressed in terms of M_2 , M_4 and M_6 as follows (Vivekanandan et al., 2004):

$$\mu = \frac{(7-11\eta) - (\eta^2 + 14\eta + 1)^{\frac{1}{2}}}{2(\eta-1)}, \quad (7)$$

$$\Lambda = \left[\frac{M_2 \Gamma(\mu+5)}{M_4 \Gamma(\mu+3)} \right]^{\frac{1}{2}}, \quad (8)$$

$$N_0 = \frac{M_k \Lambda^{\mu+l+1}}{\Gamma(\mu+l+1)}, \quad (l = 2, 4, \text{ or } 6), \quad (9)$$

where $\eta = M_4^2 / (M_2 M_6)$.

Note that N_w is identical to N_0 of the exponential size distribution given the same W and D_m as the gamma size distribution (Testud et al., 2001). In order to facilitate comparisons of the RSD parameters with those from other studies that use different distributions such as the gamma distribution, the generalized intercept parameter N_w is selected in this study. Based on the observation that the observed RSDs (Figure 7) generally follow the exponential size distribution, all RSD parameters are calculated following the exponential RSD.

2.2.2. Rain-type classification

The 34,654 1-minute interval spectra collected during the observation period are classified into three rain types: stratiform, mixed, and convective rain. For this classification, the methods of Bringi et al. (2009) and Thurai et al. (2016) are used. Bringi et al. (2009) distinguished stratiform and convective rain based on the relationship between the N_w and D_m parameters calculated from the RSD. Using a similar method, Thurai et al. (2016) found that there is a clear line of separation between those two in terms of $\log_{10} N_w$ and the median volume diameter variation. This separation line is given by:

$$\log_{10} N_w^{\text{sep}} = c_1 D_0 + c_2, \quad (10)$$

where N_w^{sep} is N_w on the separation line, c_1 is a value between -1.6 and -1.7 and c_2 is a value between 6.3 and 6.4 . The study introduces a likelihood index i to more objectively distinguish rain types, and the index i is:

$$i = \log_{10} N_w - \log_{10} N_w^{\text{sep}}. \quad (11)$$

If $i > 0.3$, the case is regarded as convective rain, and if $i < -0.3$ the case is regarded as stratiform rain. If $-0.3 \leq i \leq 0.3$, then the case is regarded

as mixed rain. In this study, if more than half of all the 1-min samples for a particular rain case correspond to a particular rain type, then that rain case is considered to have that particular rain type.

2.2.3. Weather-type classification

The key weather phenomena responsible for rain in Seoul are categorized into six groups based on surface weather maps, 850-hPa weather maps, and the weather analyses provided by KMA (Figure 6). The six weather phenomena are surface low-pressure system (L), upper-level trough (UT), southwesterly flow (SW), easterly flow (E), the Changma front (CF), and typhoon (T), each of which is treated as a separate weather type. Type L includes the cases where the surface low-pressure system passes the Korean Peninsula (Figure 6a). Type UT includes the cases in which rain occurs over the Korean Peninsula under the influence of the 500–300 hPa upper-level trough (Figure 6b). In general, the 500–300 hPa upper-level troughs have a great influence on the development of lower-level cyclones. Type SW includes the cases where relatively warm and humid low-level air of the east coast of China meets with relatively cold and dry upper-level air over the Korean Peninsula (Figure 6c). Likewise, type E includes the cases where the relatively warm and humid low-level air from the East Sea meets the relatively cold and dry upper-level air over the Korean Peninsula (Figure 6d). There is a typhoon hitting eastern Japan; however, since the center of the

typhoon is far from Seoul, it is not considered a typhoon case. The heavy rain throughout East Asia from June to July is called the Changma in Korea, and the stationary front accompanied by the Changma is called the Changma front. In this study, the case in which the stationary front stayed over the Korean Peninsula and rained toward the end of August is also classified as type CF (Figure 6e). In addition, type T is one of the types that causes heavy rain during summer on the Korean Peninsula. The cases in which the center of a typhoon is located at or near the Korean Peninsula are assigned type T. In Figure 6f, the center of Typhoon Solik is located at the East Sea. The distance between Seoul and the typhoon center is approximately 200 km, but considering the size of the typhoon, Seoul is well within the impact zone. The number of rain events classified according to these criteria is 34 events for type UT, 23 events for type CF, 20 events for type L, 9 events for type T, 8 events for type SW, and 6 events for type E.

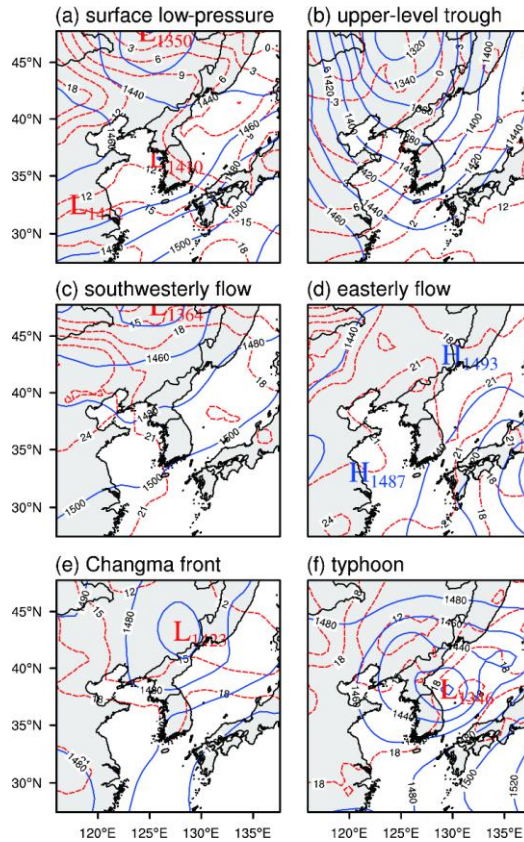


Figure 6. Synoptic weather charts at 850-hPa level describing each weather type. (a) surface low-pressure system at 15 LST 6 May 2018, (b) upper-level trough at 15 LST 26 Oct 2018, (c) southwesterly flow at 15 LST 24 Jul 2019, (d) easterly flow at 15 LST 28 Jul 2018, (e) Changma front at 21 LST 29 Aug 2018, and (f) typhoon at 15 LST 24 Aug 2018. The blue solid lines and the red dashed lines represent geopotential height and isotherm, respectively. The weather charts are depicted using European Centre for Medium-Range Weather Forecasts (ECMWF) Interim Re-Analysis (ERA-Interim) 6-hourly data.

3. Results

3.1. Characteristics of RSDs according to rain rate

Previous studies have shown that RSDs have different characteristics depending on rain rate (Waldvogel, 1974; Tokay and Short, 1996). To see the characteristics in Seoul, the RSDs for the six different rain rate categories (as in Figure 2) are obtained by averaging the 1-minute interval disdrometer data for each category (Figure 7). N_0 and Λ corresponding to the mean RSD for each category are calculated using Eqs. (5) and (6) and determine the exponential distribution. For all rain rate categories, the number concentration increases rapidly up to 0.562 mm in diameter and then decreases. For a given diameter of 0.812 mm or greater, the number concentration increases with increasing rain rate. These results are consistent with previous studies (Niu et al., 2010; Chen et al., 2017; Wu et al., 2019). Note that the discontinuity of the RSD for the first rain rate category in Figure 7 (isolated black dot) is caused by the fact that no data exist for diameters over 5 mm except for the few with diameters between 6–7mm. The exponential distributions are overall good representations of the RSDs although how well they are represented varies depending on the rain rate category.

Figure 8 shows the relationship between the RSD parameters and R . Figure 8a show that as R increases, Λ decreases. The relationship between R and Λ in Figure 8a is well represented by the power-law relationship $\Lambda = aR^b$ with $a = 4.03$ and $b = -0.20$. The intercept parameter fluctuates with rain

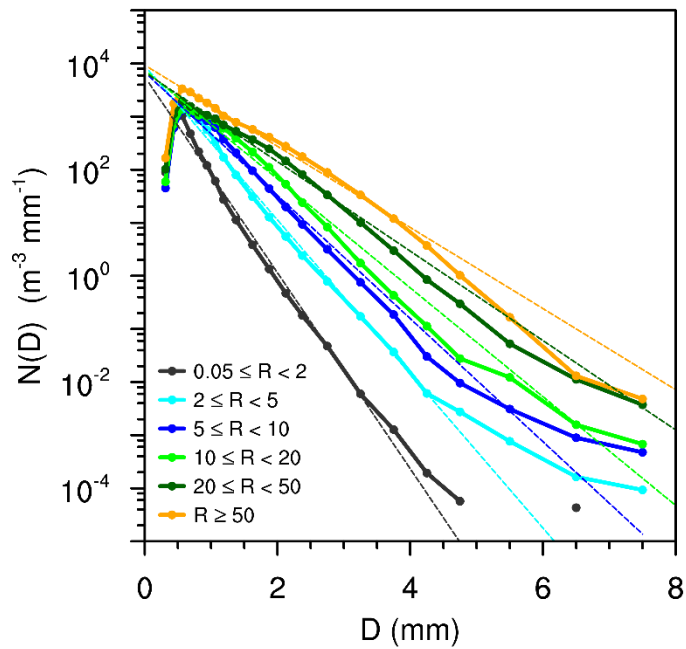


Figure 7. Raindrop size distributions (solid lines) and corresponding exponential distribution (dashed lines) for each rain rate category for the observation period.

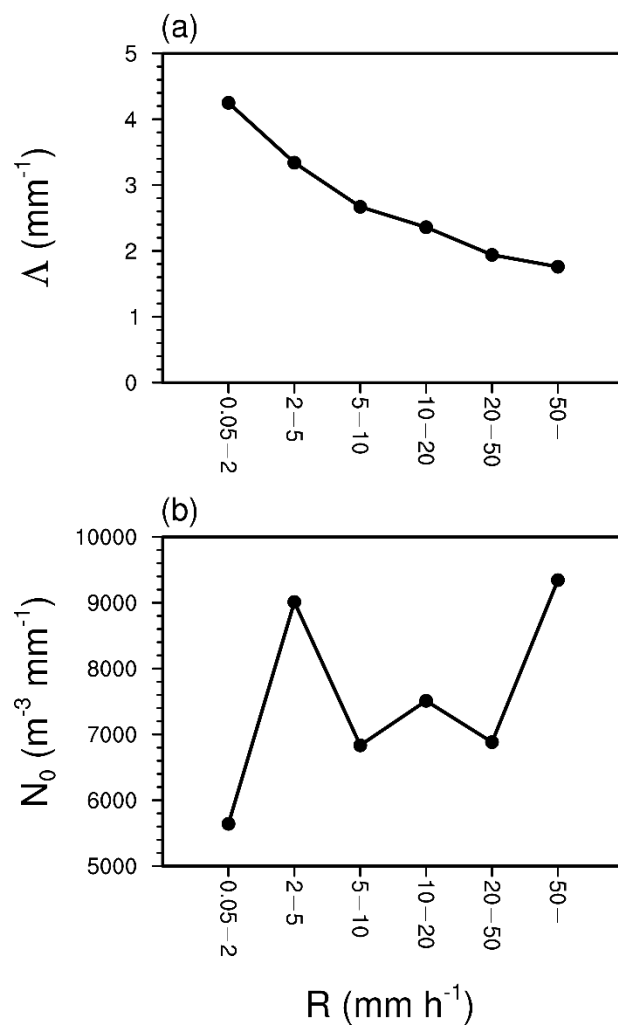


Figure 8. (a) Slope parameter and (b) intercept parameter for each rain rate category.

Table 1. Rain case number, period, rain duration, amount, type and weather type for the nine different cases (S: stratiform rain, M: mixed rain, C: convective rain).

Case no.	Period	Duration (min)	Amount (mm)	Rain type	Weather type
1	2018.05.17, 01:00 LST – 02:34 LST	95	0.3	S	SW
2	2019.02.03 17:24 LST – 19:18 LST	115	2.5	S	L
3	2019.04.14 08:51 LST – 11:02 LST	132	1.6	S	UT
4	2018.07.02, 07:58 LST – 08:31 LST	34	3.8	M	T
5	2018.11.08, 15:28 LST – 23:34 LST	487	43.1	M	L
6	2019.07.28, 11:38 LST – 12:15 LST	38	3.5	M	CF
7	2018.07.02, 09:41 LST – 10:08 LST	28	25.4	C	T
8	2018.07.02, 21:05 LST – 21:41 LST	37	13.3	C	T
9	2018.08.28, 15:53 LST – 16:53 LST	61	29.9	C	CF

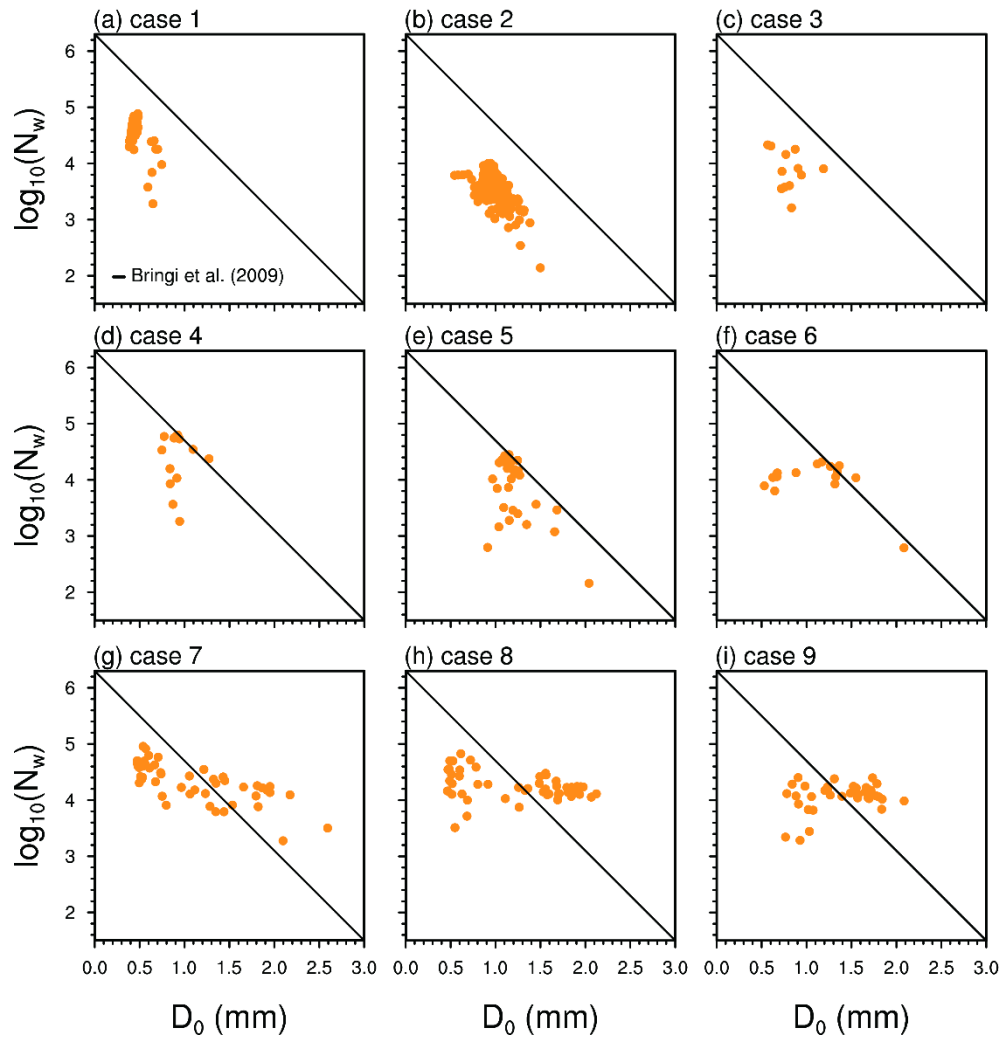


Figure 9. Scatterplots of D_0 and $\log_{10}N_w$ for rain case 1 to rain case 9. The black solid line represents the separator line of Bringi et al. (2009).

rate (Figure 8b). In particular, the N_0 values for the rain rate categories $2 \text{ mm h}^{-1} \leq R < 5 \text{ mm h}^{-1}$ and $R \geq 50 \text{ mm h}^{-1}$ are 13% and 17% larger than the constant N_0 from MP48, respectively. Unlike MP48, where only stratiform rain is considered, this study also considers mixed and convective rain. This might have contributed to the fact that the power-law relationship in this study has the a and b slightly smaller in magnitude than those in MP48 as well as the fluctuation in N_0 not seen in MP48.

3.2. Characteristics of RSDs according to different rain types

Rain events are classified into stratiform, mixed, and convective rain events according to the classification method described in section 2.2, and nine representative rain cases are selected. Table 1 summarizes rain case number, rain duration, amount, type and weather type of each case. The D_0 – $\log_{10}N_w$ relationship for each rain case is shown in Figure 9. Figures 9a–9c show stratiform rain events with an index i being smaller than 0.3, and Figures 9d–9f show mixed rain events with the index i being in the range of $-0.3 \leq i \leq 0.3$. Figures 9g–9i show convective rain events with the calculated likelihood index i being greater than 0.3. Figure 9 shows that most stratiform rain points are distributed below the line, most mixed rain points are distributed around the line, and most convective rain points are distributed above the separator line

Figure 10a shows the RSDs of stratiform rain cases, which have the

steepest slopes and the narrowest spectral widths compared with those of the mixed and convective rain cases. The RSDs of convective rain cases have the most modest slopes and the widest spectral widths (Figure 10c). In particular, the RSD of case 3 that corresponds to stratiform rain event has narrower width and higher raindrop number concentration at the peak than cases 1 and 2. For mixed rain cases, the RSDs have characteristics that fall between those of convective and stratiform rain cases (Figure 10b).

Figure 11 shows the probability density functions (PDFs) of the RSD parameters D_m , $\log_{10}N_w$, Λ , and Z . The mean value of D_m for stratiform rain is 0.92 mm, which is smaller than that for convective rain (1.55 mm). Mixed rain (1.40 mm) has a mean value between those for stratiform and convective rain, but the mean value is much closer to that of convective rain. Stratiform rain has a relatively narrow range of D_m with small PDF dispersion, whereas convective rain has a wider range of D_m (Figure 11a).

For $\log_{10}N_w$, the mean values of stratiform, mixed, and convective rain are 3.86, 3.82, and 4.06 $\text{m}^{-3} \text{mm}^{-1}$, respectively. The PDF shape of convective rain is relatively narrow, while the PDF shape of stratiform rain is relatively broad (Figure 11b). Contrary to the results of D_m , the mean value of $\log_{10}N_w$ for mixed rain is quite similar to that for stratiform rain.

The mean values of Λ for stratiform, mixed, and convective rain are 4.40, 2.76, and 2.71 mm^{-1} , respectively, which is consistent with the differences in spectral widths for each type, as shown in Figure 10. The PDFs

of convective and mixed rain have a smooth distribution with one peak near the mean value (Figure 11c). The PDF of stratiform rain has the flattest and widest shape with multiple peaks.

The mean value of Z for convective rain is 36.9 dBZ, which is large compared to the Z values for the other two types of rain (32.8 and 19.1 dBZ). Since Z is directly related to the total number concentration and is proportional to D_m to the power of 6 (Steiner et al., 2004), Z is used as an indicator of the number concentration of large raindrops. Therefore, stratiform (convective) rain with the smallest (largest) Z has few (many) raindrops with large diameters. As in the PDF of D_m , the differences in the three rain types are clearly visible in Z (Figure 11d). Approximately 87% of stratiform rain events are distributed below 30 dBZ, ~75% of convective rain events are distributed above 30 dBZ, and ~64% of mixed rain events are distributed in the range of $30 \text{ dBZ} < Z < 40 \text{ dBZ}$.

Overall, the PDFs of D_m and $\log_{10}N_w$ of the convective rain show positive skewness and the stratiform rain tends to be opposite, which is the common RSD characteristic of the two rain types seen in previous studies (Chen et al., 2013; Ji et al., 2019). It is noteworthy, however, that the mean value of D_m is smaller and $\log_{10}N_w$ is larger compared to previous studies that have considered other climatic regions such as Darwin, Australia (Bringi et al., 2009) and Beijing, northern China (Ji et al., 2019). Another point to note is that the observed stratiform rain shows a broad range of $\log_{10}N_w$ and

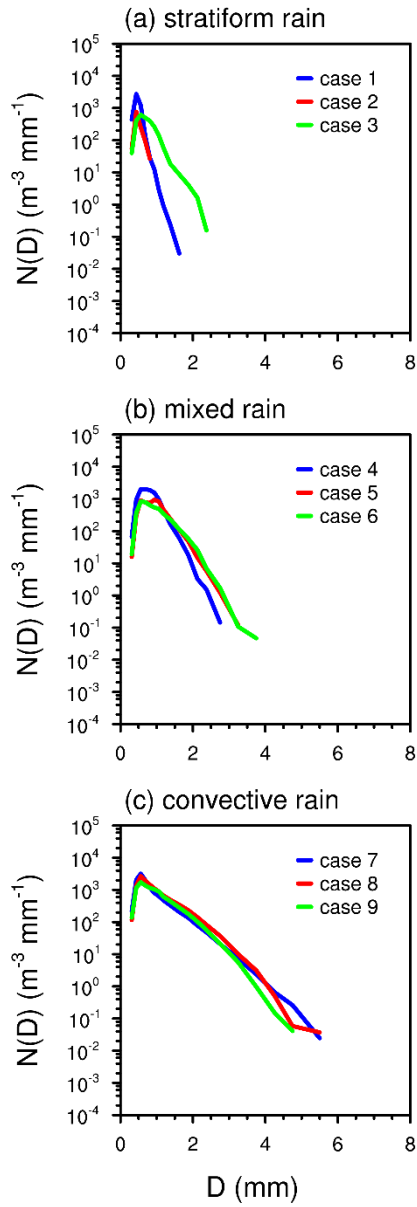


Figure 10. Raindrop size distributions for each rain case during (a) stratiform rain (case 1, case 2, and case 3), (b) mixed rain (case 4, case 5, and case 6), and (c) convective rain cases (case 7, case 8, and case 9).

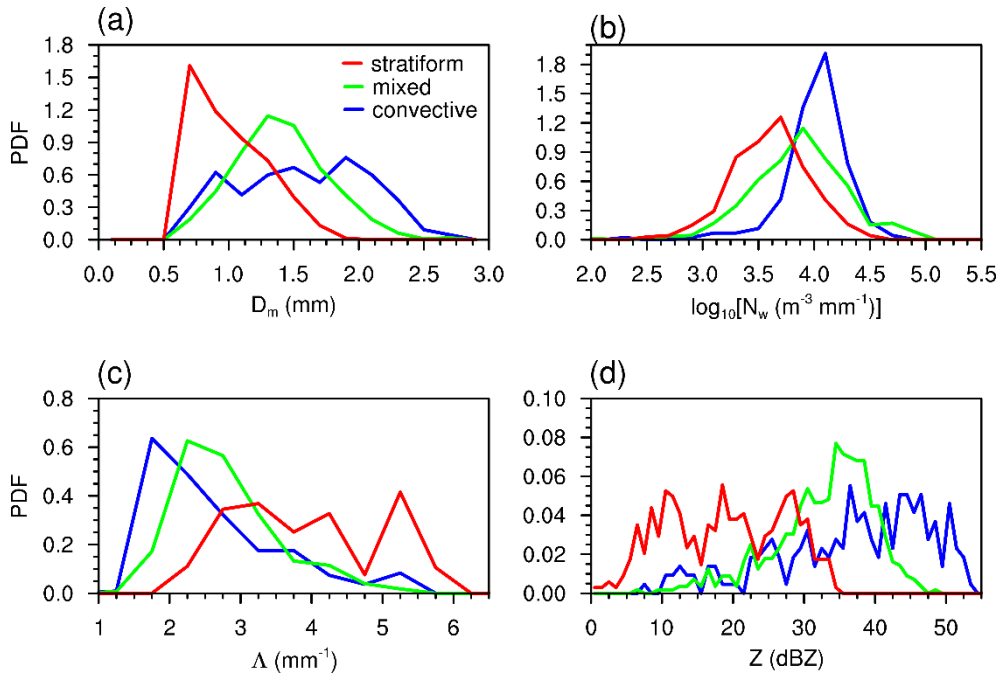


Figure 11. Probability density functions of (a) D_m , (b) $\log_{10}N_w$, (c) Λ , and (d) Z for each rain type.

Λ , which indicates the diversity of RSD forms for stratiform rain in Seoul. This may be related to various weather types that affect Seoul.

3.3. Characteristics of RSDs according to different weather types

In this section, the observed characteristics of the RSD for different weather types are examined. Figure 12 shows the mean RSD for the six different weather types. The difference between the RSDs is not apparent below a diameter of 1.25 mm, but the number concentration of small raindrops is smallest for type E. As the diameter increases, the raindrop number concentration for type E and SW decreases slowly, whereas that for type L and UT decreases fast. The raindrop number concentration for type CF and T shows a moderate decrease. The RSD for type E contains the greatest number concentration for raindrops larger than 4.5 mm in diameter, followed by SW, CF, UT, T, and L. The maximum raindrop diameter for type E is approximately 8 mm.

Figure 13 shows the PDF of the RSD parameters for the six weather types. The statistical values for each parameter are also compared (Table 2). The mean value of D_m for type L events is 0.95 mm, which is the smallest value among the values of the six weather types. The PDFs of D_m all display positive skewness, which means that the distributions are biased toward the small diameter range and have peaks in the range of 0.65–1.25 mm (Figure 13a). In addition, the PDFs for type L and UT are concentrated within

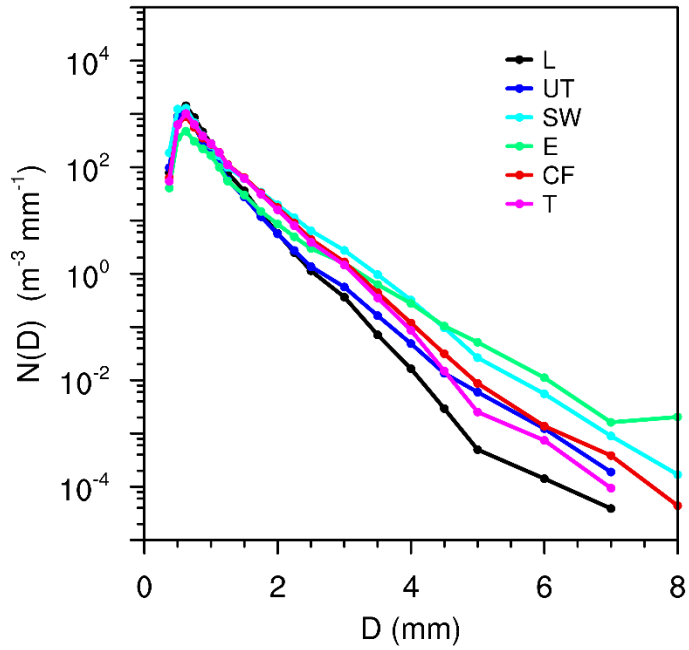


Figure 12. Raindrop size distributions for each weather type (L: surface low-pressure system, UT: upper-level trough, SW: southwesterly flow, E: easterly flow, CF: Changma front, and T: typhoon).

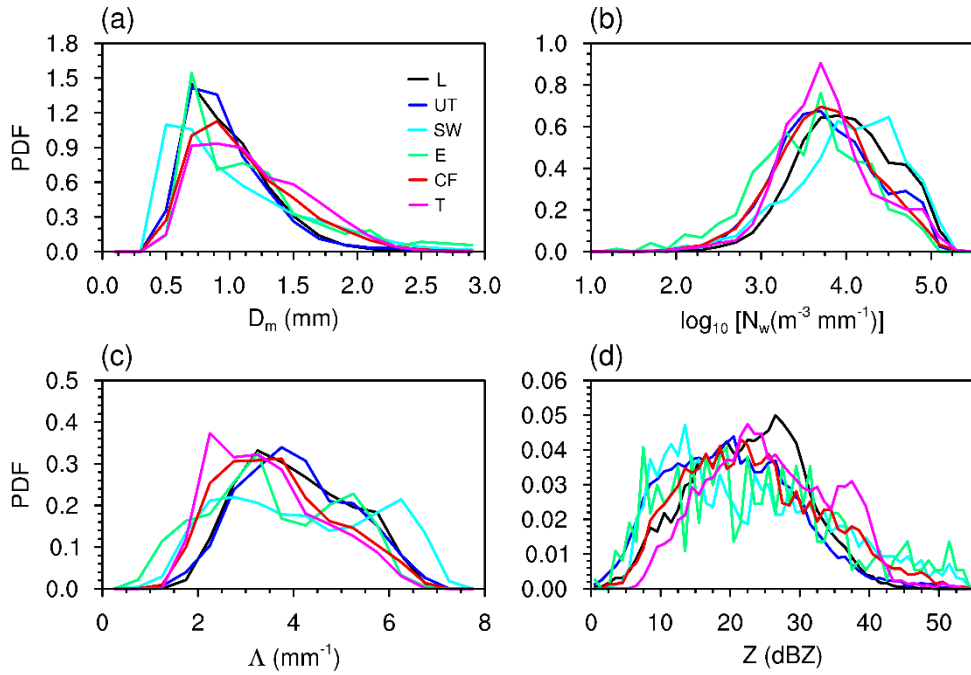


Figure 13. Probability density functions of (a) D_m , (b) $\log_{10} N_w$, (c) Λ , and (d) Z for each weather type (L: surface low-pressure system, UT: upper-level trough, SW: southwesterly flow, E: easterly flow, CF: Changma front, and T: typhoon).

Table 2. Mean (μ), standard deviation (σ), kurtosis (k), and skewness (s) of D_m , $\log_{10}N_w$, Λ , and Z PDFs for different weather types. Squared brackets indicate averaging over the PDF of all daily rain events classified according to weather types.

Weather type		D_m	$\log_{10}N_w$	Λ	Z
L	$[\mu]$	0.95	3.96	4.23	20.9
	$[\sigma]$	0.23	0.40	0.79	6.2
	$[k]$	1.19	-0.42	-0.88	-0.46
	$[s]$	1.07	-0.15	0.18	-0.02
UT	$[\mu]$	1.02	3.70	3.93	20.3
	$[\sigma]$	0.32	0.46	0.90	8.5
	$[k]$	8.80	-0.25	-0.59	-0.11
	$[s]$	2.03	-0.03	0.18	0.38
SW	$[\mu]$	1.13	3.73	3.87	22.0
	$[\sigma]$	0.42	0.53	1.05	9.0
	$[k]$	3.88	0.21	-1.02	-0.46
	$[s]$	1.55	-0.51	0.28	0.38
E	$[\mu]$	1.54	3.30	2.97	27.0
	$[\sigma]$	0.58	0.55	1.00	10.6
	$[k]$	3.46	0.03	-0.90	-0.52
	$[s]$	1.79	-0.52	-0.22	0.50
CF	$[\mu]$	1.14	3.66	3.70	22.5
	$[\sigma]$	0.36	0.45	0.88	7.8
	$[k]$	7.72	0.17	-0.57	-0.40
	$[s]$	1.57	-0.19	0.43	0.42
T	$[\mu]$	1.12	3.76	3.59	24.1
	$[\sigma]$	0.27	0.41	0.73	6.7
	$[k]$	-0.38	0.30	-0.54	-0.65
	$[s]$	0.59	0.18	0.56	0.15

relatively small D_m values with small standard deviation values of 0.23 and 0.32, respectively, while type E and SW show large standard deviation values of D_m with 0.58 and 0.42, respectively.

Figure 13b shows the PDF of $\log_{10}N_w$. The mean value of $\log_{10}N_w$ for type E is $3.30 \text{ m}^{-3} \text{ mm}^{-1}$, which is relatively small compared to those of other weather types. Given the small $\log_{10}N_w$, type E has a relatively large PDF value. On the other hand, given the large $\log_{10}N_w$, type L has a relatively large PDF value. The kurtosis value of $\log_{10}N_w$ for type CF is greater than 0, which means that the distributions have heavier tails compared to the normal distribution. The PDF for type CF appears to be something of a middle ground between the type E and L PDFs.

To better compare the difference in D_m and $\log_{10}N_w$ for the six weather types, the D_m - $\log_{10}N_w$ boxplot is given (Figure 14). The separation line in Bringi et al. (2003) represents an inverse relationship between D_m and $\log_{10}N_w$ for stratiform rain. Since the median values of D_m - $\log_{10}N_w$ for all weather types lie below the line, every weather type consists of a large proportion of stratiform rain compared to convective rain. Some differences can still be found in the distribution of data considering the 10th and 90th percentiles. Large portions of the distributions of type L and UT events belong to the category of stratiform rain with negligible proportions of convective rain 0.6% and 1.9%, respectively. The median values of D_m for both types are almost identical, but type L event shows a relatively large

median value of $\log_{10}N_w$. Type L rain is characterized by small raindrops with a relatively large raindrop number concentration.

The percentages of convective rain for type T and CF are 2.6% and 5.6% of the total, respectively, which are relatively larger than those of type L and UT events. The median of D_m for type T and CF events exhibit larger values than that for type L and UT events. In both types, D_m - $\log_{10}N_w$ pairs close to the maritime cluster are observed. The result is consistent with the differences in each PDF shown in Figure 13a.

Both type E and SW events show the largest proportions of convective rain (14.6 and 8.8%, respectively). While much of the D_m - $\log_{10}N_w$ distribution for type SW events occupies a maritime cluster, the distribution for type E events occupies both maritime and continental clusters. Comparing types E and SW, type E rain is characterized by larger raindrops with a relatively low raindrop number concentration similar to the characteristic of continental convective rain. The RSD of the continental cluster is defined as being characterized by lower concentrations of larger raindrops than the RSD of the maritime cluster (Bringi et al., 2003).

Figure 13c shows the PDF of Λ . The mean values of Λ cover the range of 2.97–4.23 mm^{-1} , and the standard deviations all fall in 0.70–1.10 mm^{-1} . The peak values of Λ for convective and mixed rain are 1.75 and 2.25 mm^{-1} , and several peak values for stratiform rain are included in the range of 3.25–6.25 mm^{-1} (Figure 11c). Comparing these values with the mean values

of Λ for the six weather types, it can be seen that the type E and SW are closer in characteristics to convective rain, while types CF and T events and types L and UT events are closer to mixed rain and stratiform rain, respectively.

The PDFs of Z for all weather types are shown in Figure 13d. The PDFs of Z also indicate that each weather type consists of a mixture of stratiform and convective rain, so raindrops of various sizes can be observed. Figure 15 shows the scatterplot between Z and R for total observation data and the fitted power-law relationship for each weather type. There is a difference in the coefficient and exponent of each fitted power-law relationship, and the difference is more pronounced when R is small. Type E has the largest coefficient among all weather types and the exponent close to 1. In contrast, type CF has the smallest coefficient and the largest exponent. The large value of the exponent for type CF events means that the variation of R over type CF events is greatly affected by the variation of the number of large raindrops.

It is worth noting that each of the types UT, CF, and L, which recorded larger numbers of events during the observation period, has its distinctive RSD characteristics. The mean D_m and $\log_{10}N_w$ of type UT events are 1.02 mm and $3.70 \text{ m}^{-3} \text{ mm}^{-1}$, respectively, with larger D_m and smaller $\log_{10}N_w$ compared to those of type L events (0.95 mm and $3.96 \text{ m}^{-3} \text{ mm}^{-1}$), suggesting that these two types related to the low-pressure system

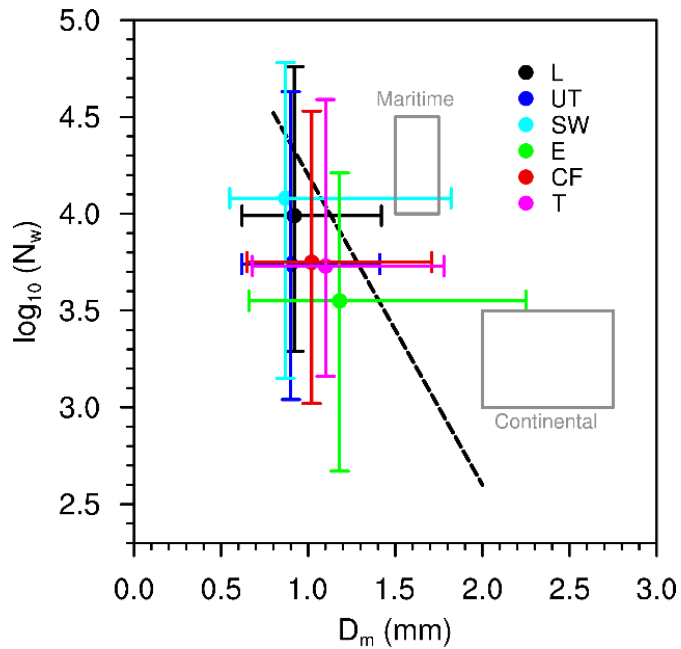


Figure 14. Boxplot of D_m - $\log_{10}N_w$ pairs (medians with 10th and 90th percentiles) for each weather type (L: surface low-pressure system, UT: upper-level trough, SW: southwesterly flow, E: easterly flow, CF: Changma front, and T: typhoon). The black dashed line represents the stratiform line in Bringi et al. (2003). The two gray boxes indicate the maritime and continental convective clusters, respectively, reported by Bringi et al. (2003).

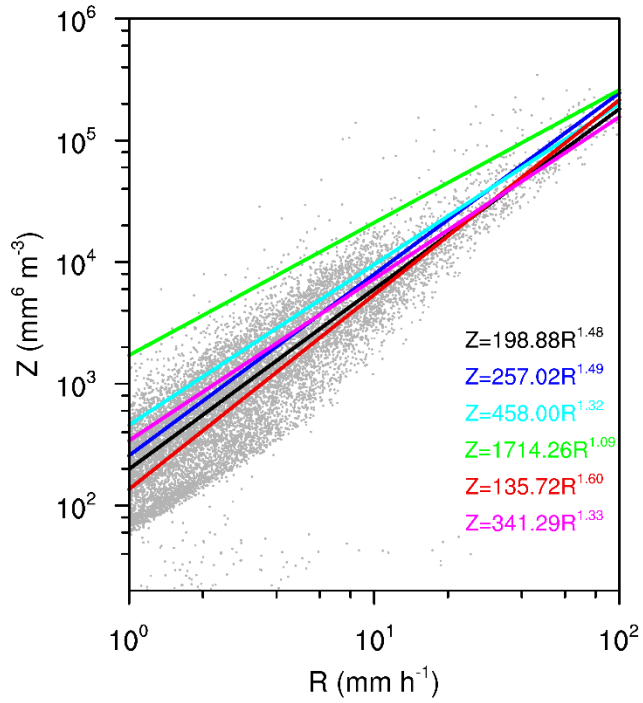


Figure. 15. Scatterplot of Z - R pairs for each weather type (L: surface low-pressure system, UT: upper-level trough, SW: southwesterly flow, E: easterly flow, CF: Changma front, and T: typhoon). The fitted power-law relationship $Z=aR^b$ for each weather type are indicated by black, blue, cyan, green, red, and magenta solid lines, respectively.

differ in RSD characteristics. The type CF events have a smaller mean value of $\log_{10}N_w$ compared to the type UT events but have a larger mean D_m (D_m is 1.14 mm and $\log_{10}N_w$ is $3.66 \text{ m}^{-3} \text{ mm}^{-1}$). The distributions of $\log_{10}N_w$ between the two types are nearly similar, but that of D_m is wider for type CF. This means that the value of D_m observed in Seoul during the Changma period is highly variable. Moreover, a large portion of the type CF distribution occupies maritime clusters compared to those of type UT and L, which indicates that the convective rain associated with the Changma front in Korea is close to maritime nature.

The East Asian summer monsoon is known as the Changma in Korea, Baiu in Japan, and Meiyu in China. Chen et al. (2013) shows larger mean D_m and smaller $\log_{10}N_w$ (1.40 mm and $3.55 \text{ m}^{-3} \text{ mm}^{-1}$), while Wen et al. (2017) shows larger mean D_m and higher mean $\log_{10}N_w$ (1.27 mm and $3.79 \text{ m}^{-3} \text{ mm}^{-1}$) for the East Asian summer monsoon cases. In both studies, the convective rain caused by the Meiyu front over eastern China is close to maritime in nature. In Chen et al. (2019), which observed raindrops by Baiu front in Tokyo, Japan, the mean value of D_m is 1.15 mm and $\log_{10}N_w$ is $3.59 \text{ m}^{-3} \text{ mm}^{-1}$, which is similar to mean D_m but smaller in $\log_{10}N_w$ for type CF events. The results show that even with the similar weather types, the RSD characteristics can vary from region to region.

The sounding data from a nearby location are examined to compare the differences in cloud characteristics for the six weather types. Table 3

shows the lifted condensation level (LCL), level of free convection (LFC), equilibrium level (EL), convective available potential energy (CAPE), and precipitable water averaged for each weather type using upper-air soundings at Osan station during the observation period. The mean LCL is examined to approximate the cloud base height, and the mean LFC, EL, and CAPE are calculated to estimate the potential of cloud development. Type E events have a mean LCL of approximately 742 m AGL and a mean EL of 9941 m AGL. The mean

CAPE from the type E events have a value of 1062 J kg^{-1} . These indicate that the clouds can develop to high altitudes due to the strong vertical instability of the atmosphere, which can cause intense rainfall. This might have affected the generation of large raindrops in type E events. Type CF events also show a relatively large mean CAPE compared to other type events but is relatively smaller than type E events. Comparing the sounding parameters of type L and UT events highlights the differences. Commonly, they show relatively low mean EL, CAPE and precipitable water compared to other type events. The differences in the sounding parameters of type L and UT events seem to be related to the differences in their RSD results (Figures 15 and 16). Nonetheless, further investigation is needed to determine which microphysical processes actually produce raindrops that can be observed in these weather types.

Clouds for specific weather type events are analyzed using upper-air soundings from Osan station and Communication, Ocean and Meteorological

Satellite (COMS) cloud-top temperature data (Figures 15 and 16). The rain events selected for comparison are a surface low-pressure system (type L) at 09 LST on 6 May 2018, an easterly flow (type E) at 21 LST on 28 Jul 2018, and a Changma front (type CF) at 21 LST on 29 Aug 2018, which are identical to the rain events in Figure 6. Since the clouds cover both Seoul and Osan station at the same time, the sounding from Osan station can be used for the analysis conducted for Seoul regarding the rain events selected in this study (Figure 17).

The skew T - $\log p$ diagrams in Figure 16b show that the easterly wind blows from the surface to 850-hPa, and this layer is warmer than the upper layer. Since the upper layer is relatively cold and dry, vertical instability occurs with significant CAPE, which is likely a factor in the formation of large raindrops. Figure 17b shows that the cloud-top temperature for the type E event is approximately 228 K with thick clouds developing locally at approximately 11.5 km AGL. The LCL for the type E event is approximately 700 m AGL, and a relatively long distance from the surface may have affected the decrease in the number concentration of small raindrops via evaporation process (Figure 12).

The LCL for the type L event is approximately 500 m AGL (Figure 16a), and the cloud-top temperature is approximately 248 K (Figure 17a). This means that the type L cloud begins to develop at very low altitudes and grows into relatively low clouds. The number of small raindrops for this weather type is higher than that for other weather types as in the RSD of type

L shown in Figure 12.

Figure 16c shows the skew T - $\log p$ diagrams for the type CF rain event. The temperature and dew point temperature profiles show that the atmosphere is quite humid. The LCL for the type CF event is relatively low at approximately 500 m AGL. Moreover, the cloud-top temperature is approximately 228 K (Figure 17c), so the cloud top height is expected to be high. Type CF rain is likely to have large concentrations of small raindrops due to the low cloud base height and the significant concentration of large raindrops due to a well-developed cloud (You et al. 2010).

Table 3. Mean values of lifted condensation level (LCL), level of free convection (LFC), equilibrium level (EL), convective available potential energy (CAPE), and precipitable water calculated from 368 Osan station soundings of each weather type.

Weather type	LCL (m AGL)	LFC (m AGL)	EL (m AGL)	CAPE (J kg ⁻¹)	Precipitable water (mm)
L	492	554	1916	17	21.8
UT	620	670	3123	85	24.6
SW	548	764	7395	363	44.8
E	742	1000	9941	1062	50.5
CF	438	477	8615	649	51.2
T	363	438	5874	248	55.1

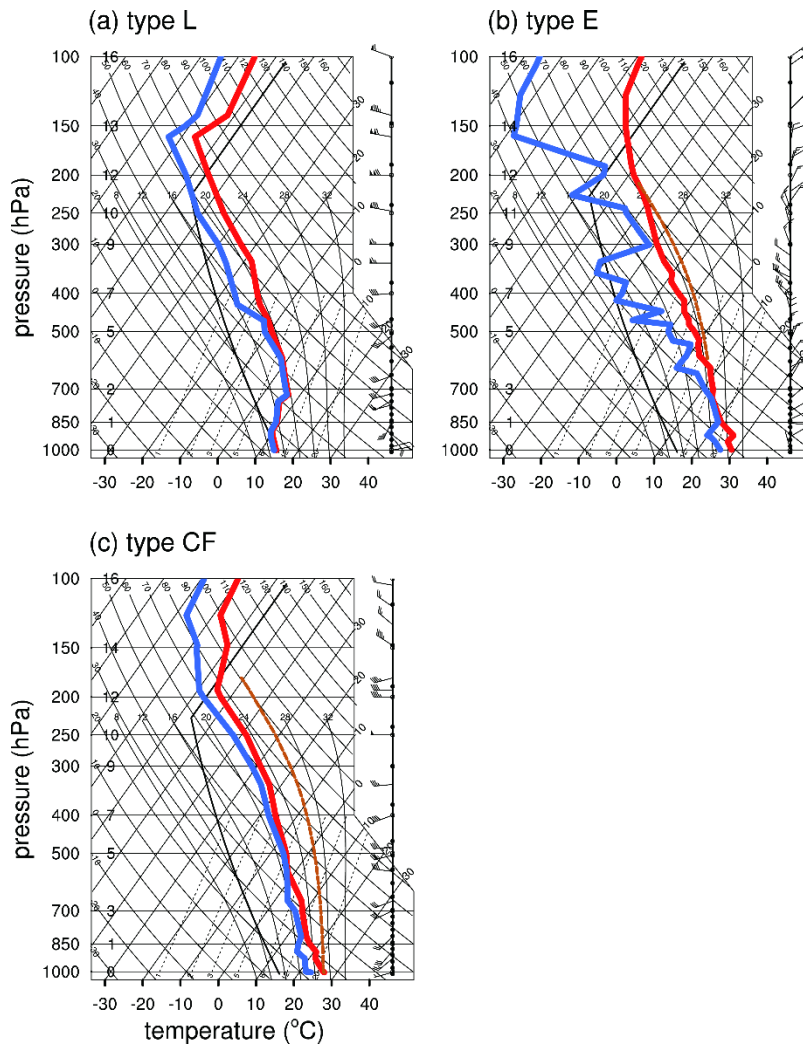


Figure 16. Skew T - $\log p$ diagrams of Osan station soundings during the event of (a) surface low-pressure system at 09 LST 6 May 2018, (b) easterly flow at 21 LST 28 Jul 2018, and (c) Changma front at 21 LST 29 Aug 2018. The solid red and blue lines are temperature and dew point temperature profiles, respectively. The brown line indicates the moist adiabatic lapse rate connecting LFC and EL. Wind barbs are plotted on the right side of the soundings.

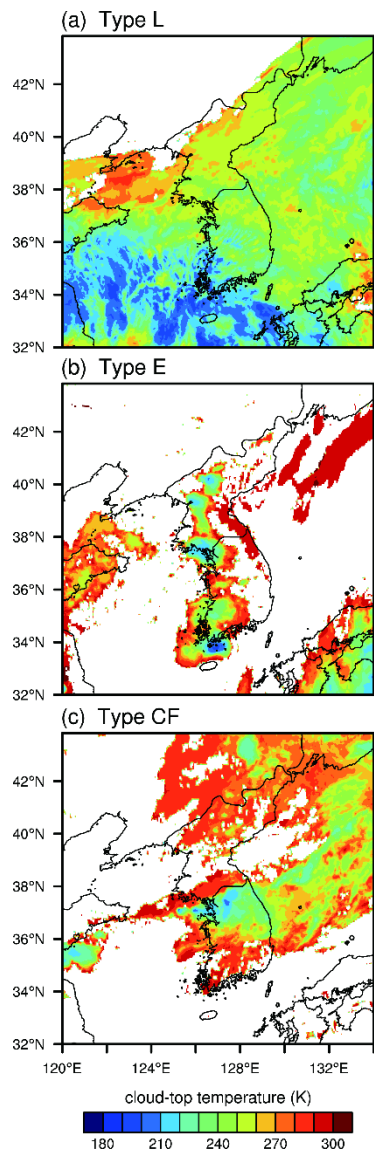


Figure 17. Cloud-top temperature (K) for the same event of figure 16 using National Meteorological Satellite Center (NMSC) COMS data.

3.4. Application to the numerical models

3.4.1. Parameterization of the intercept parameter

The results in section 3.1 show that the observed N_0 is far from constant and varies considerably with R . Wang et al. (2018) derived Λ - N_0 relationships for convective and stratiform rain samples, reporting very different distributions of N_0 for the two different rain types. Efforts have been made to represent N_0 as a function of an appropriate RSD parameter rather than a constant. Zhang et al. (2008) derived a relationship between W and N_0 by using a statistical relation between two RSD moments and found that applying the W - N_0 relationship to the numerical model has the potential to improve rain estimation. Wainwright et al. (2014) derived W - N_0 relationship using the model calculations obtained by Milbrant and Yau (2005) double-moment simulations of the tornadic supercell event and found that the model with the single-moment microphysics scheme where the W - N_0 relationship is employed showed a simulation result closer to the double-moment scheme than the model using the N_0 constant. Wang et al. (2016) derived Λ - N_0 relation to replace the N_0 constant, and found that the estimation of precipitation intensity based on the relation showed higher accuracy than the estimation based on the constant N_0 assumptions.

Scatterplots of Λ and N_0 and scatterplots of W and N_0 are shown in Figures 18a and 18b respectively. Although the relationship

between each parameter is not clear because of high dispersion, in general, as the value of the parameter on the x -axis increases, the value of the parameter on the y -axis tends to increase. The relationships can be used for the parameterization of the raindrop size distribution in single-moment bulk microphysics schemes. Using the Levenberg-Marquardt nonlinear least-squares method, N_0 is represented as a simple function of W and Λ ($N_0=17176 \times W^{0.2886}$ and $N_0=545.53 \times \Lambda^{2.04}$), respectively. In this study, the W - N_0 relationship is used to parameterize N_0 because N_0 has a large dependency on W .

However, it is hard to explain N_0 with only one equation because the dispersion of data is large and the dispersion tends to be different depending on the range of R (figure not shown). Therefore, based on the result of Tokay and Short (1996), this study classified the data into three rain types according to the range of R . The data in the range of $R < 1 \text{ mm h}^{-1}$ is stratiform rain and $10 \text{ mm h}^{-1} \leq R$ is convective rain. The data corresponding to $1 \text{ mm h}^{-1} \leq R < 10 \text{ mm h}^{-1}$ is named mixed rain. Table 4 shows N_0 expressed as a function of W for each rain type. The total data consists of 55% of stratiform rain, 41% of mixed rain, and 4% of convective rain. Figures 19a–19c show the W - N_0 scatterplot and the fitted power-law relationships ($N_0=1130000 \times W^{1.82}$, $N_0=7173 \times W^{0.24}$, and $N_0=28810 \times W^{0.63}$) for stratiform, mixed, and convective rain, respectively. R^2 for each rain type is 0.54, 0.03, and 0.09, respectively. Given that R^2 is -0.04 when

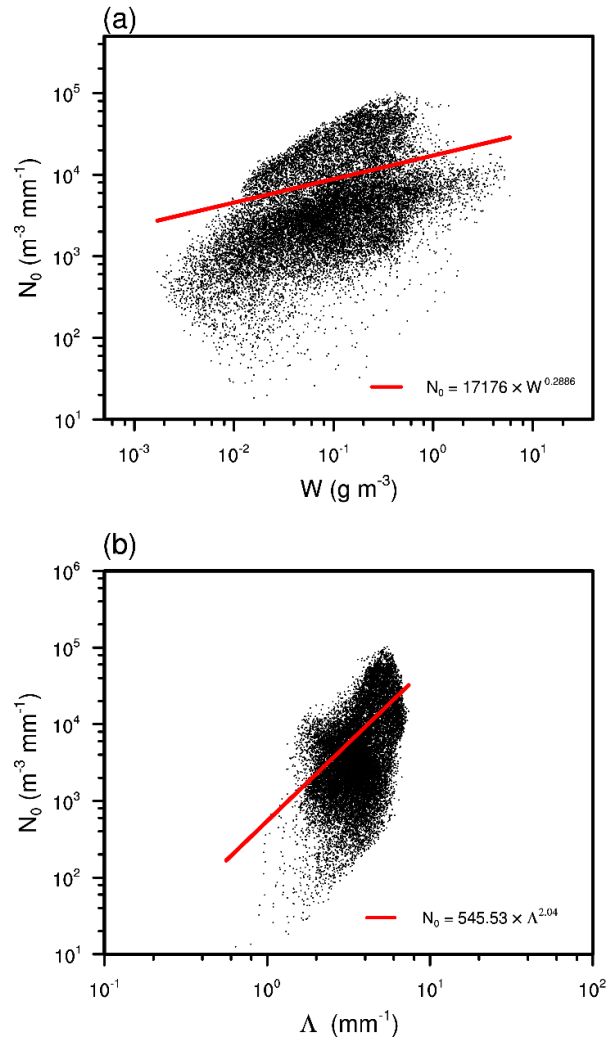


Figure 18. Intercept parameter as a function of (a) rainwater content and (b) slope parameter for the entire 1-min rain samples (black dots). Red lines represent fitted power law equations.

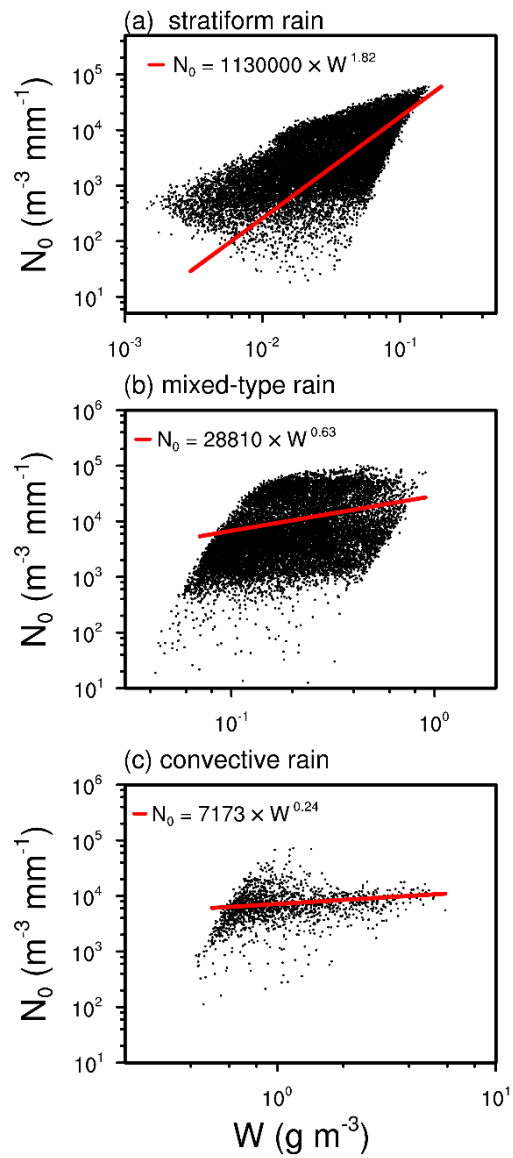


Figure 19. Intercept parameter as a function of rainwater content for (a) stratiform, (b) mixed, and (c) convective rain. Red lines represent fitted power law equations.

Table 4. Description of intercept parameter types and corresponding value /equations.

Type		Value / Equation
	Constant N_0	8000 [$\text{m}^{-3} \text{mm}^{-1}$]
	Stratiform rain	$N_0=1130000 \times W^{1.82}$
Power law	Mixed rain	$N_0=28810 \times W^{0.63}$
	Convective rain	$N_0=7173 \times W^{0.24}$

$N_0 = 8000 \text{ m}^{-3}\text{mm}^{-1}$, the $W-N_0$ relationships according to rain types better describes the rain characteristics than a single N_0 .

3.4.2. Experiment settings

In this study, the Weather Research and Forecasting (WRF) version 3.9.1 model is used. The model domain configuration and the physics schemes used in numerical simulation are presented in Figure 20 and Table 5. Three two-way nested domains are used with the horizontal resolutions of 27, 9, and 3 km. 50 model levels in the vertical direction are considered. The model time step in domain 1 is 90 seconds, and in the internal domain it is reduced to a third of each, 30 seconds and 10 seconds respectively. National Centers for Environmental Predictions (NCEP) Global Data Assimilation system (GDAS) Final Global Analysis (FNL) 0.25-degree reanalysis data are used as the initial and boundary conditions. Model integrations are performed for 30 hours starting from 03 LST August 29 2018, and the initial 3 hours are regarded as the model spin-up time. The real case simulations are conducted to see if the scheme with newly derived $W-N_0$ relationships (WSM6 modified) improves precipitation estimation over the WRF Single-Moment 6-class Microphysics (WSM6) scheme.

Before simulating the main experiment, the subsidiary experiment is conducted to determine how to apply the $W-N_0$ relationships according to rain types to the WSM6 scheme. The $W-N_0$ relationships are derived from

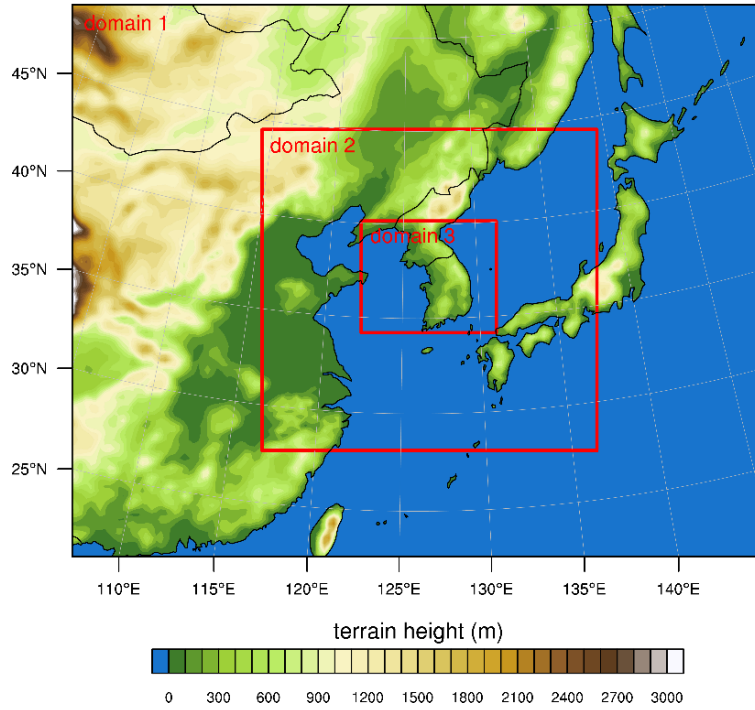


Figure 20. Illustration of three nested model domains with terrain height.

Table 5. Domain configuration and physics schemes used in this study.

	Domain1	Domain2	Domain3
Horizontal grid size (km)	27	9	3
Horizontal grid number	150×120	217×208	262×217
Vertical grid number		50	
Time step (s)	90	30	10
Planetary boundary layer	Yonsei University Scheme (Hong et al., 2006)		
Shortwave radiation	Dudhia scheme (Dudhia, 1989)		
Longwave radiation	Rapid radiative transfer model (Mlawer et al., 1997)		
Land surface	Unified Noah land surface model (Tewari et al., 2004)		
Subgrid-scale cumulus	Kain-Fritsch scheme (Kain, 2004)		none
Microphysics	WRF Single-Moment 6-class Microphysics Scheme (Hong and Lim, 2006)		
Initial/boundary conditions	NCEP GDAS/FNL 0.25-degree analysis		

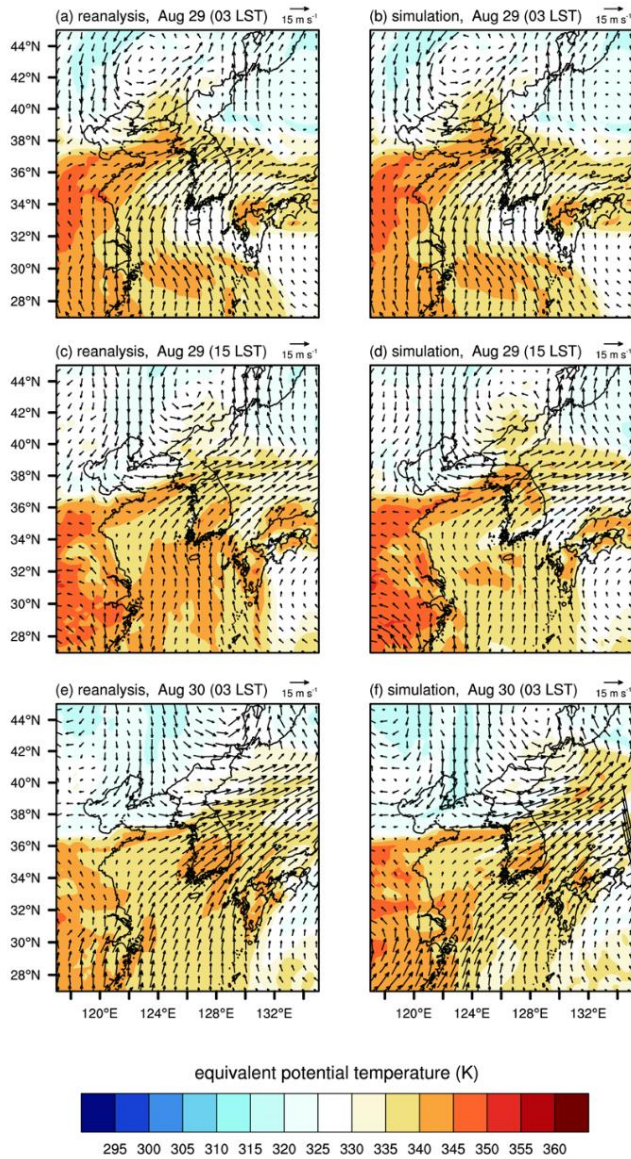


Figure 21. Fields of 850 hPa equivalent potential temperature (K, shaded) and horizontal wind vector (m s^{-1} , arrows) at (a) Aug 29 03 LST, (c) Aug 29 15 LST and (e) Aug 30 03 LST using the National Centers for Environmental Prediction (NCEP) Final (FNL) 0.25-degree analysis data. Same for (b), (d), (f) but from simulation results.

disdrometer data collected at the surface. However, if the relationships at the surface are applied to all vertical levels of the model, simulation results that are less realistic can be obtained. Therefore, the experiment is conducted with the following four options of calculating R used to classify the rain type and W of each relationship into model levels. Considering the vertical column at a specific x point, the rain type is classified by R at the surface, and W can be calculated differently for each model level in the relationship of corresponding rain type (Option 1). W can also be calculated as a value on the surface (Option 2). If W is zero at the surface, the value with the smallest W in the same column can be used for the calculation. Alternatively, the mean value of W , calculated at all model levels in the column, can be applied to W (Option 3). Finally, R can be calculated at all model levels to classify rain types, and different relationships are applied to each level, and W of the relationship can be also calculated for each level (Option 4). Each option is applied to the WSM6 modified scheme to determine which of these options simulates the most realistic precipitation.

To verify the experiment settings, the equivalent potential temperature and the horizontal wind at 850 hPa for the reanalysis data and model results were compared at 12-hour intervals (Figure 21). The equivalent potential temperature and the horizontal wind patterns show that warm and humid air flows to the Korean Peninsula from the southeastern coast of China. Cold and dry air from the upper air of China blows southwards, encountering

warm and humid air over the Korean Peninsula, creating vertical instability leading to a large amount of precipitation (figure not shown). According to the result, the model can be expected to predict the precipitation location well because the patterns in the reanalysis data and the model results generally match around the Korean Peninsula. But over time, the speed and location of the wind field passing through the Korean Peninsula show a slight difference, which may influence the simulation result.

3.4.3. Numerical model results

Figures 22c–22f show spatial distributions of the surface precipitation amount accumulated over the 57-hour period from 00 LST August 28 2018 to 09 LST August 29 2018 for four different R and W options. The surface precipitation amount accumulated over the 57-hour period of the Tropical Rainfall Measuring Mission (TRMM) satellite observations (Figure 22a) and the AWS observations (Figure 22b) are presented. The spatial distribution of surface precipitation amount in Figure 22b is shown using ground observations from AWS installed in South Korea, but only part of the distribution is represented, so the overall distribution was confirmed using TRMM satellite observations. Two observation results show that the precipitation event forms a precipitation zone centered on the Korean Demilitarized Zone (DMZ), and it rained heavily to the north of Seoul. It is also confirmed that it rained in parts of the south and north of Gangwon-do.

Comparing the simulation results with the two observations, the pattern in Figure 22c of Option 1 and Figure 22f of Option 4 matches well with the two observation patterns. Both simulation results show better precipitation amount in the north of Seoul, compared to Figures 22d and 22e. The Brier score (Brier, 1950) for 57-hour accumulated surface precipitation amount is calculated over a threshold range to assess the performance of the model simulations. The lower the Brier score, the better the simulation performance. Figure 23 shows that Option 4 performs well in the threshold range of 40–70 mm, but Option 1 performs the best in the most of the threshold range. Therefore, WSM6 and WSM6 modified schemes with Option 1 are used for precipitation estimation.

Figures 24c–24d show the results of a real case simulation where Option 1 are applied to the WSM6 and WSM6 modified schemes. A 24-hour accumulated surface precipitation amount of TRMM (Figure 24a) and AWS observations (Figure 24b) is presented for comparison. Figures 24c–24d seem to match well with the spatial distribution of accumulated precipitation amount shown in the observations. However, the maximum peak in Figure 24c appears at locations not observed in Figures 24a–24b. The maximum peak in Figure 24d is well represented, except for some over-estimated parts. Moreover, Figure 24d shows a better distribution of accumulated precipitation amount of less than 320 mm compared to Figure 24c. The WSM6 modified scheme shows an RMSE of 70.9 mm, which is lower than that of the WSM6 scheme (78.6 mm). The model performance of the WSM6

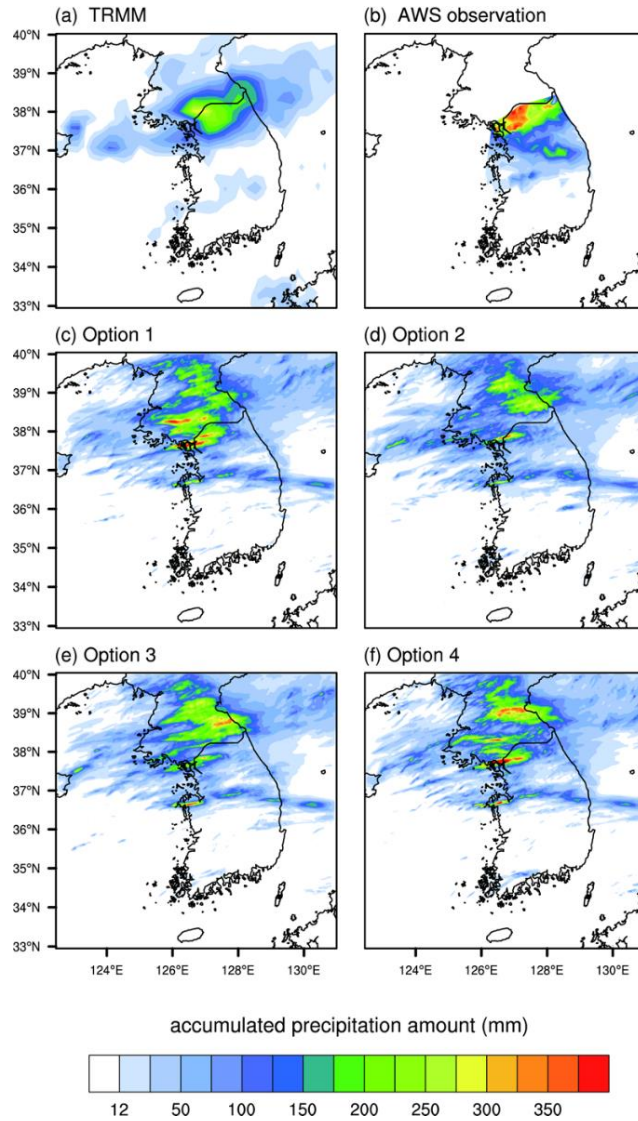


Figure 22. (a) Spatial distributions of the surface precipitation amount accumulated over the 57-h period of TRMM satellite observations and (b) AWS observations, and (c) ~ (f) WRF simulation results for four different rain rate and rainwater content.

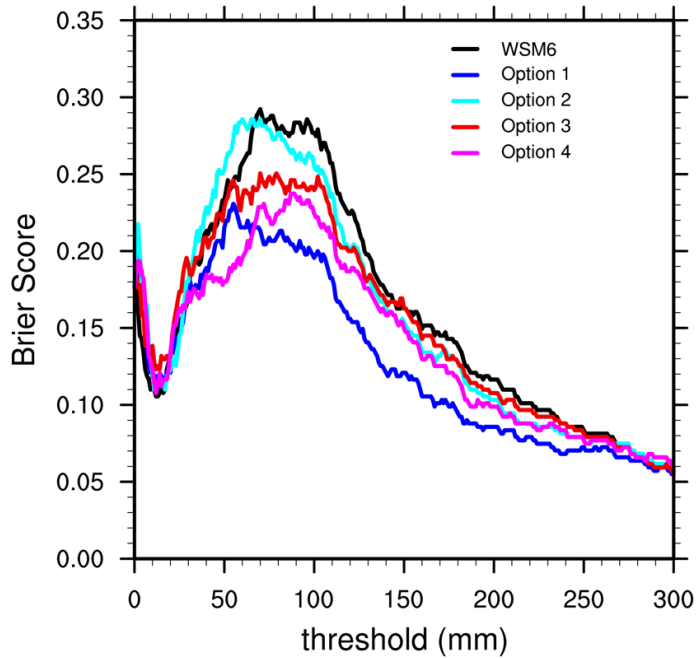


Figure 23. The Brier score for the 57-h accumulated precipitation amount of each rain rate and rainwater content option (Option1~4) across the range of thresholds. The Brier score for WSM6 scheme is also depicted for comparison.

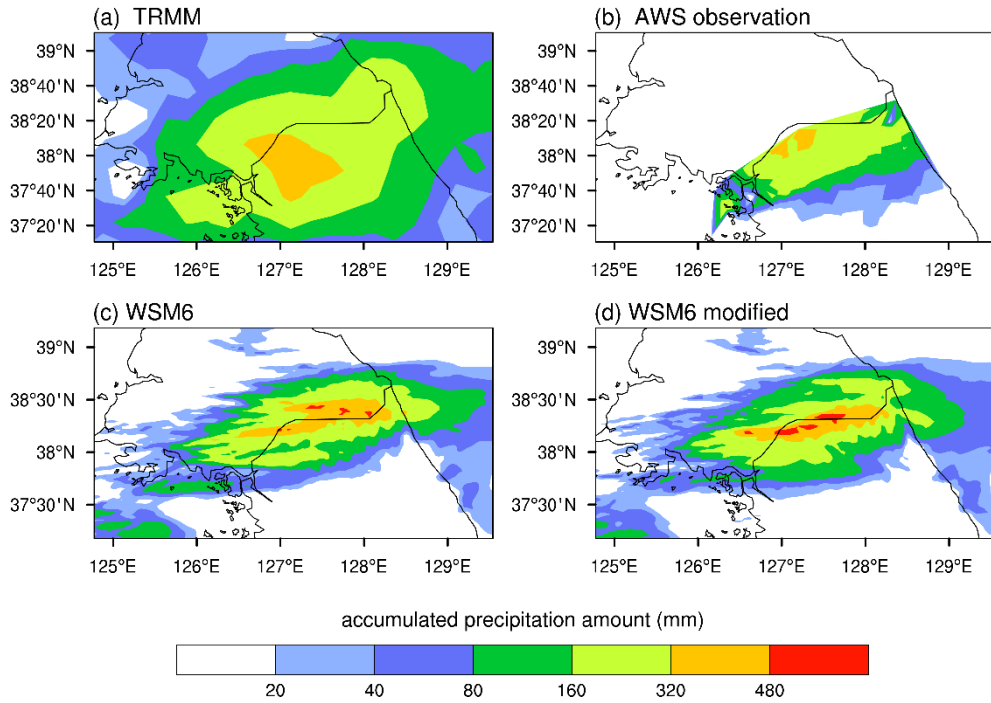


Figure 24. (a) Spatial distributions of the surface precipitation amount accumulated over the 24-h period of TRMM satellite observations, (b) AWS observations, (c) WSM6 scheme, and (d) WSM6 modified scheme.

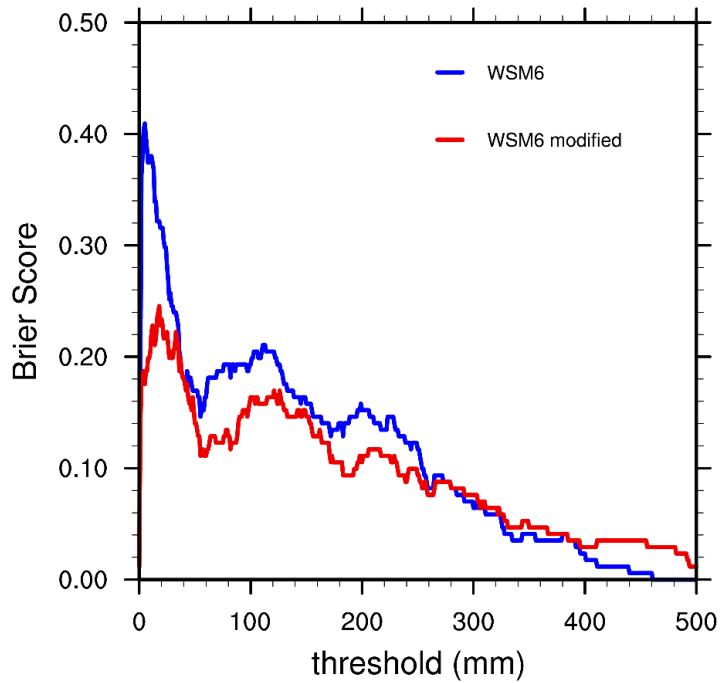


Figure 25. The Brier score for the 24-h accumulated precipitation amount of each parameterization (WSM6 scheme and WSM6 modified scheme) across the range of thresholds.

modified scheme is excellent overall, but shows better performance than the WSM6 scheme, especially at threshold smaller than 280 mm (Figure 25). For this precipitation case, the numerical model with the WSM6 modified scheme using the $W-N_0$ relationships according to the rain types better simulates the surface precipitation than the numerical model with the original WSM6 scheme.

4. Summary and Discussions

In this study, the RSD characteristics in Seoul are examined according to rain and weather types using the raindrop spectra measured by the Parsivel² disdrometer from May 2018 to July 2019. The measured data are the first RSD observations in Seoul. The disdrometer data are validated through comparison with the AWS rain gauge data and are quality-controlled by removing unreliable data resulting from measurement inaccuracies.

The RSDs in Seoul are subdivided according to rain intensities. For all rain intensities, the RSDs for $D \geq 0.562$ mm are well represented by the exponential distribution. The slope parameter of the exponential size distribution is in a power-law relation with the rain intensity ($\Lambda = 4.03R^{-0.20}$). The intercept parameter of the exponential size distribution varies considerably with the rain intensity, which does not agree with MP48's finding.

The RSDs are classified into three rain types, stratiform, mixed, and convective rain, using the D_0 – $\log_{10}N_w$ relationship. As in many previous studies, the RSDs for stratiform rain are characterized by the steepest slope and the smallest D_m and Z , while the RSDs for convective rain are characterized by the most modest slopes and the largest D_m , $\log_{10}N_w$, and Z . However, $\log_{10}N_w$ and Λ for stratiform rain in Seoul show significantly broad distributions, which is not commonly found in previous studies about other climatic regions. These characteristic in distributions are thought to originate from different manifestations of stratiform rain associated with the diverse weather patterns affecting Seoul. The RSDs of mixed rain show the mean values of D_m and Λ close to those of convective rain and the mean value of $\log_{10}N_w$ close to that of stratiform rain.

The RSD characteristics of different weather types I in Seoul are examined. The RSDs of type L is characterized by the steepest slope, the smallest mean value of D_m , the largest mean value of $\log_{10}N_w$, and the smallest proportion of convective rain among the weather types. Type UT, which exhibits the second to the smallest proportion of convective rain among all weather types, shows also the second to the smallest mean value of D_m , which is close to that of type L. Type UT, however, is characterized by the mean value of $\log_{10}N_w$ rather close to that of other weather types such as SW and CF. The RSD characteristics of type CF show a middle of the pack level of convective rain proportion and mean values of D_m , $\log_{10}N_w$, and Λ

but the largest exponent of the $Z-R$ power-law relation, which implies that the rain intensity of type CF highly depends on the production of large raindrops. The RSDs of type E are characterized by having the greatest proportion of convective rain among all weather types as well as the largest D_m and the smallest $\log_{10}N_w$ and Λ .

The thermodynamic sounding data and satellite data collected from a nearby location are analyzed for each weather type. The mean values of CAPE for type CF and E are large ($> 600 \text{ J kg}^{-1}$) while those for type L and UT are very small ($< 100 \text{ J kg}^{-1}$). The large thermodynamic instability of type CF and E which can induce vigorous convection may be responsible for the relatively large convective rain proportions of type CF and E compared to those of type L and UT.

The intercept parameters according to the rain type are parameterized for use in a numerical model. The data are classified into three rain types according to the range of R . The fitted power-law relationships are represented as $N_0=1130000 \times W^{1.82}$, $N_0=7173 \times W^{0.24}$, and $N_0=28810 \times W^{0.63}$ for stratiform, mixed, and convective rain, respectively. It is shown that the representation of N_0 as a function of W explains the rain characteristics better than the constant N_0 of MP48.

The real case simulation is performed to verify that the three $W-N_0$ relationships broken down into the rain types improve precipitation estimation over the WSM6 scheme. In order to get more realistic simulation

results, preliminary model experiments are first conducted to determine the model level at which R and W are calculated in the model. The most realistic precipitation appears when the rain type is classified by R at the surface and W is calculated differently for each model level. The simulated 24-hour accumulated surface precipitation amount is compared with the TRMM satellite observations and the AWS observations and shows that the numerical model with the WSM6 modified scheme better simulates the surface precipitation than the numerical model with the original WSM6 scheme.

Further in-depth studies on the dynamical and microphysical processes in the precipitation systems corresponding to each of these weather types are needed to provide more detailed explanations for the different RSD characteristics of these weather types. In addition, a longer-term RSD data from more than one station are needed to formulate a more general parameterization of N_0 for use in numerical models with the goal of robustly improving precipitation estimation across the entire Korean Peninsula.

References

- Atlas, D., Srivastava, R. C., & Sekhon, R. S. (1973). Doppler radar characteristics of precipitation at vertical incidence, *Review of Geophysics*, *11*, 1–35.
- Atlas, D., & Ulbrich, C. W. (2000). An observationally based conceptual model of warm oceanic convective rain in the tropics, *Journal of Applied Meteorology*, *39*, 2165–2181.
- Barthazy, E., Gölke, S., Schefold, R., & Högl, D. (2004). An optical array instrument for shape and fall velocity measurements of hydrometeors, *Journal of Atmospheric and Oceanic Technology*, *21*, 1400–1416.
- Brier, G. W. (1950). Verification of forecasts expressed in terms of probability, *Monthly Weather Review*, *78*, 1–3.
- Bringi, V. N., Chandrasekar, V., Hubbert, J., Gorgucci, E., Randeu, W. L., & Schoenhuber, M. (2003). Raindrop size distribution in different climatic regimes from disdrometer and dual-polarized radar analysis, *Journal of Atmospheric Sciences*, *60*, 354–365.
- Bringi, V. N., Williams, C. R., Thurai, M., & May, P. T. (2009). Using dual-polarized radar and dual-frequency profiler for DSD characterization: A case study from Darwin, Australia, *Journal of Atmospheric and Oceanic Technology*, *26*, 2107–2122.
- Chang, W., Wang, T. C., & Lin, P. (2009). Characteristics of the raindrop size

distribution and drop shape relation in typhoon systems in the western Pacific from the 2D video disdrometer and NCU C-band polarimetric radar, *Journal of Atmospheric and Oceanic Technology*, 26, 1973–1993.

Chen, B., Hu, Z., Liu, L., & Zhang, G. (2017). Raindrop size distribution measurements at 4,500 m on the Tibetan Plateau during TIPEX-III, *Journal of Geophysical Research: Atmospheres*, 122, 11092–11106.

Chen, B., Wang, Y., & Ming, J. (2012). Microphysical characteristics of the raindrop size distribution in typhoon Morakot (2009), *Journal of Tropical Meteorology*, 18, 162–171.

Chen, B., Yang, J., & Pu, J. (2013). Statistical characteristics of raindrop size distribution in the meiyu season observed in Eastern China, *Journal of the Meteorological Society of Japan*, 91, 215–227.

Chen, Y., Duan, J., An, J., & Liu, H. (2019). Raindrop size distribution characteristics for tropical cyclones and Meiyu-Baiu fronts impacting Tokyo, Japan, *Atmosphere*, 10, 391.

Dudhia, J. (1989). Numerical study of convective observed during the winter monsoon experiment using a mesoscale two-dimensional model, *Journal of the Atmospheric Sciences*, 46, 3077–3107.

Friedrich, K., Karlina, E. A., Masters, F. J., & Lopez, C. R. (2013). Drop-size distributions in thunderstorms measured by optical disdrometers during VORTEX2, *Monthly Weather Review*, 141, 1182–1203.

Gao, W., Liu, L., Li, J., & Lu, C. (2018). The microphysical properties of

- convective precipitation over the Tibetan Plateau by a subkilometer resolution cloud-resolving simulation, *Journal of Geophysical Research: Atmospheres*, *123*, 3212–3227.
- Ghada, W., Buras, A., Lüpke, M., Schunk, C., & Menzel, A. (2018). Rain microstructure parameters vary with large-scale weather conditions in Lausanne, Switzerland, *Remote Sensing*, *10*, 811.
- Hanchani, S., Boudevillain, B., Delrieu, G., & Bargaoui, Z. (2017). Drop size distribution climatology in Cévennes-Vivarais region, France, *Atmosphere*, *8*, 233.
- Hong, S. Y., & Lim, J. J. (2006). The WRF Single-Moment 6-class microphysics scheme, *Journal of the Korean Meteorological Society*, *42*, 129–151.
- Hong, S. Y., Noh, Y., & Dudhia, J. (2006). A new vertical diffusion package with an explicit treatment of entrainment processes, *Monthly Weather Review*, *134*, 2318–2341.
- Jaffrain, J., & Berne, A. (2011). Experimental quantification of the sampling uncertainty associated with measurements from PARSIVEL disdrometers, *Journal of Hydrometeorology*, *12*, 352–370.
- Ji, L., Chen, H., Li, L., Chen, B., Xiao, X., Chen, M., & Zhang, G. (2019). Raindrop size distributions and rain characteristics observed by a PARSIVEL disdrometer in Beijing, Northern China, *Remote Sensing*, *11*, 1479.
- Kain, J. S. (2004). The Kain-Fritsch convective parameterization: An update,

Journal of Applied Meteorology, 43, 170–181.

- Kozu, T., Shimomai, T., Akramin, Z., Marzuki, Shibagaki, Y., & Hashiguchi, H. (2005). Intraseasonal variation of raindrop size distribution at Koto Tabang, West Sumatra, Indonesia, *Geophysical Research Letters*, 32, L07803.
- Krajewski, W. F., Kruger, A., Caracciolo, C., Golé, P., Barthes, L., Creutin, J., Delahaye, J., Nikolopoulos, E. I., Ogden, F., & Vinson, J. (2006). DEVEX-disdrometer evaluation experiment: Basic results and implications for hydrologic studies, *Advances in Water Resources*, 29, 311–325.
- Leinonen, J., Moisseev, D., Leskinen, M., & Petersen, W. A. (2012). A climatology of disdrometer measurements of rainfall in Finland over five years with implications for global radar observations, *Journal of Applied Meteorology and Climatology*, 51, 392–404.
- Loh, J. L., Lee, D. I., & You, C. H. (2019). Inter-comparison of DSDs between Jincheon and Miryang at South Korea, *Atmospheric Research*, 227, 52–65.
- Marshall, J. S., Palmer, & W. McK. (1948). The distribution of raindrops with size, *Journal of Meteorology*, 5, 165–166.
- Massmann, A. K., Minder, J. R., Garreaud, R. D., Kingsmill, D. E., Valenzuela, R. A., Montecinos, A., Fults, S. L., & Snider, J. R. (2017). The Chilean coastal orographic precipitation experiment: observing the influence of microphysical rain regimes on coastal orographic

- precipitation, *Journal of Hydrometeorology*, 18, 2723–2743.
- Milbrant, J. A., & Yau, M. K. (2005). A multimoment bulk microphysics parameterization. Part II: A proposed three-moment closure and scheme description. *Journal of Atmospheric Sciences*, 62, 3065–3081.
- Mlawer, E. J., Taubman, S. J., Brown, P. D., Iacono, M. J., & Clough, S. A. (1997). Radiative transfer for inhomogeneous atmospheres: RRTM, a validated correlated-k model for the longwave, *Journal of Geophysical Research*, 102, 16663–16682.
- Montopoli, M., Marzano, F. S., & Vulpiani, G. (2008). Analysis and synthesis of raindrop size distribution time series from disdrometer data, *Geoscience and Remote Sensing*, 46, 466–478.
- Niu, S., Jia, X., Sang, J., Liu, X., Lu, C., & Liu, Y. (2010). Distributions of raindrop sizes and fall velocities in a semiarid plateau climate: Convective versus stratiform rains. *J. Appl. Meteorol. Climatol.* 49, 632–645.
- Rosenfeld, D., & Ulbrich, C. W. (2003). Cloud microphysical properties, processes, and rainfall estimation opportunities, *A collection of essays in honor of David Atlas (Meteorological Monographs)*, 30, 237–258.
- Sreekanth, T. S., Hamza, V., Resmi, E. A., & Mohan K. G. (2019). Classification and seasonal distribution of rain types based on surface and radar observations over a tropical coastal station, *Atmospheric Research*, 218, 90–98.
- Steiner, M., Smith, J. A., & Uijlenhoet, R. (2004). A microphysical

- interpretation of radar reflectivity-rain rate relationships, *Journal of the Atmospheric Sciences*, *61*, 1114–1131.
- Suh, S. H., You, C. H., & Lee, D. I. (2016). Climatological characteristics of raindrop size distributions in Busan, Republic of Korea, *Hydrology and Earth System Sciences*, *20*, 193–207.
- Tapiador, F. J., Checa, R., & De Castro, M. (2010). An experiment to measure the spatial variability of rain drop size distribution using sixteen laser disdrometers, *Geophysical Research Letters*, *37*, L16803.
- Tenorio, R. S., Christina da Silva Moraes, M., & Sauvageot, H. (2012). Raindrop size distribution and radar parameters in coastal tropical rain systems of northeastern Brazil, *Journal of Applied Meteorology and Climatology*, *51*, 1961–1970.
- Testud, J., Oury, S., Black, R. A., Amayenc, P., & Dou, X. (2001). The concept of “normalized” distribution to describe raindrop spectra: A tool for cloud physics and cloud remote sensing, *Journal of Applied Meteorology*, *40*, 1118–1140.
- Tewari, M., Chen, F., Wang, W., Dudhia, J., LeMone, M. A., Mitchell, K., et al. (2004). Implementation and verification of the unified NOAA land surface model in the WRF model. *20th Conference on Weather Analysis and Forecasting/16th Conference on Numerical Weather Prediction*, pp. 11–15.
- Thompson, E. J., Rutledge, S. A., Dolan, B., & Thurai, M. (2015). Drop size distributions and radar observations of convective and stratiform rain

- over the equatorial Indian and west Pacific Oceans, *Journal of the Atmospheric Sciences*, 72, 4091–4125.
- Thurai, M., Bringi, V. N., & May, P. T. (2010). CPOL radar-derived drop size distribution statistics of stratiform and convective rain for two regimes in Darwin, Australia, *Journal of Atmospheric and Oceanic Technology*, 27, 932–942.
- Thurai, M., Gatlin, P. N., & Bringi, V. N. (2016). Separating stratiform and convective rain types based on the drop size distribution characteristics using 2D video disdrometer data, *Atmospheric Research*, 169, 416–423.
- Tokay, A., & Short, D. A. (1996). Evidence from tropical raindrop spectra of the origin of rain from stratiform versus convective clouds, *Journal of Applied Meteorology*, 35, 355–371.
- Tokay, A., Wolff, D. B., & Petersen, W. A. (2014). Evaluation of the new version of the laser-optical disdrometer, OTT Parsivel², *Journal of Atmospheric and Oceanic Technology*, 31, 1276–1288.
- Ulbrich, C. W. (1983). Natural variations in the analytical form of the raindrop size distribution, *Journal of Climate and Applied Meteorology*, 22, 1764–1775.
- Ulbrich, C. W., & Atlas, D. (2007). Microphysics of raindrop size spectra: Tropical continental and maritime storms, *Journal of Applied Meteorology and Climatology*, 46, 1777–1791.
- Vivekanandan, J., Zhang, G., & Brandes, E. (2004). Polarimetric radar

- estimators based on a constrained gamma drop size distribution model, *Journal of Applied Meteorology*, *43*, 217–230.
- Waldvogel, A. (1974). The N_0 jump raindrop spectra, *Journal of Atmospheric Sciences*, *31*, 1067–1078.
- Wainwright, C. E., Dawson, D. T., Xue, M., & Zhang, G. (2014). Diagnosing the intercept parameters of the exponential drop size distributions in a single-moment microphysics scheme and impact on supercell storm simulations, *Journal of Applied Meteorology and Climatology*, *53*, 2072–2090.
- Wang, J., Dong, X., & Xi, B. (2018). Investigation of liquid cloud microphysical properties of deep convective systems: 2. Parameterization of raindrop size distribution and its application for convective rain estimation, *Journal of Geophysical Research: Atmospheres*, *123*, 11637–11651.
- Wang, J., Dong, X., Xi, B., & Heymsfield, A. J. (2016). Investigation of liquid cloud microphysical properties of deep convective systems: 1. Parameterization of raindrop size distribution and its application for stratiform rain estimation, *Journal of Geophysical Research: Atmospheres*, *121*, 10739–10760.
- Wen, L., Zhao, K., Wang, M., & Zhang, G. (2019). Seasonal variations of observed raindrop size distribution in East China, *Advances in Atmospheric Sciences*, *36*, 346–362.
- Wen, L., Zhao, K., Zhang, G., Liu, S., & Chen, G. (2017). Impacts of

- instrument limitations on estimated raindrop size distribution, radar parameters, and model microphysics during Mei-Yu season in East China, *Journal of Atmospheric and Oceanic Technology*, *34*, 1021–1037.
- Wu, Z., Zhang, Y., Zhang, L., Lei, H., Xie, Y., Wen, L., & Yang, J. (2019). Characteristics of summer season raindrop size distribution in three typical regions of western Pacific. *J. Geophys. Res. Atmos.* *124*, 4054–4073.
- You, C. H., & Lee, D. I. (2015). Decadal variation in raindrop size distribution in Busan, Korea, *Advances in Meteorology*, *2015*, 329327.
- You, C. H., Lee, D. I., Jang, S. M., Jang, M., Uyeda, H., Shinoda, T., & Kobayashi, F. (2010). Characteristics of rainfall systems accompanied with Changma front at Chujado in Korea, *Asia-Pacific Journal of Atmospheric Sciences*, *46*, 41–51.
- Yuter, S. E., Kingsmill, D. E., Nance, L. B., & Löffler-Mang, M. (2006). Observations of precipitation size and fall speed characteristics within coexisting rain and wet snow, *Journal of Applied Meteorology and Climatology*, *45*, 1450–1464.
- Zhang, G., Ming, X., Cao, Q., & Dawson, D. (2008). Diagnosing the Intercept Parameter for Exponential Raindrop Size Distribution Based on Video Disdrometer Observations: Model Development, *Journal of Applied Meteorology and Climatology*, *47*, 2983–2992.
- Zhang, G., Sun, J., & Brandes, E. A. (2006). Improving parameterization of

rain microphysics with disdrometer and radar observations, *Journal of Atmospheric Sciences*, 63, 1273–1290.

Zhang, H., Zhang, Y., He, H., Xie, Y., & Zeng, Q. (2017). Comparison of raindrop size distributions in a midlatitude continental squall line during different stages as measured by Parsivel over East China, *Journal of Applied Meteorology and Climatology*, 56, 2097–2111.

초 록

본 연구에서는 2018년 5월부터 2019년 7월까지 서울에서 관측된 빗방울 크기 분포 (Raindrop size distribution, RSD)를 강수 유형과 날씨 유형으로 구분하여 분석하였다. 세 개의 강수 유형 (대류형, 혼합형, 층운형)과 6개의 날씨 유형(지표 저기압 시스템, 상층 기압골, 남서풍류, 동풍류, 장마 전선, 태풍)이 고려되었다. 강수 유형 중 층운형 강수의 RSD가 가장 급격한 기울기와 가장 작은 질량 가중 직경을 보였으며, 대류형 강수의 RSD는 이와 반대되는 특성을 보였다. 층운형 강수의 일반화된 절편 인자와 기울기 인자는 다른 강수 유형에 비해 넓은 PDF 분포를 보였으며, 이는 서울에서의 다양한 날씨 유형과 연관이 있는 것으로 생각된다. 혼합형 강수의 질량 가중 직경과 기울기 인자는 대류형 강수에서 나타난 값들과 비슷한 한편, 일반화된 절편 인자는 층운형 강수에서 나타난 값과 비슷하다. 서울 RSD 특성은 날씨 유형에 따라서도 크게 달라진다. 지표 저기압 시스템과 상층 기압골 RSD는 다른 날씨 유형에 비해 상대적으로 급격한 기울기와 적은 비중의 대류형 강수가 나타났다. 반면에 장마 전선과 동풍류의 RSD는 상대적으로 완만한 기울기와 상당한 비중의 대류형 강수가 나타났다. 연직 사운딩 자료와 위성 자료를 통해 확인된 이 두 날씨 유형의 큰 대기 불안정도가 큰 비중의 대류형 강수와 연관된 것으로 확인되었다. 장마 전선 RSD를 통해 구한 $Z-R$ 멱급수 관계식의 지수항이 다른 날씨 유형에 비해 가장 큰 것을 통해 장마 전선으로 인한 강수의 강수 강도는 큰 빗방울의 생산과 크게 연관된 것으로 생각된다. 강수 유형에 따른 우수함량과 절편인자 간의 멱급수 관계식이 벌크 미세물리 과정에

적용되었다. 수정된 벌크 미세물리 과정이 적용된 수치 모형의 강수 모의 능력이 기존의 방안이 적용된 수치 모형의 강수 모의 능력보다 전반적으로 향상된 모의 성능을 보였다.

주요어 : 빗방울 크기 분포, 디스드로미터, 강수 유형, 날씨 유형, 서울, WRF 모형, 모수화

학번 : 2017-28708